ADVANCED MATERIALS
www.advmat.de

Synergistic Pharmacological Therapy to Modulate Glial Cells in Spinal Cord Injury

*Valeria Veneruso, Emilia Petillo, Fabio Pizzetti, Alessandro Orro, Davide Comolli, Massimiliano De Paola, Antonietta Verrillo, Arianna Baggiolini, Simona Votano, Franca Castiglione, Mattia Sponchioni, Gianluigi Forloni, Filippo Rossi, and Pietro Veglianese**

Current treatments for modulating the glial-mediated inflammatory response after spinal cord injury (SCI) have limited ability to improve recovery. This is quite likely due to the lack of a selective therapeutic approach acting on microgliosis and astrocytosis, the glia components most involved after trauma, while maximizing efficacy and minimizing side effects. A new nanogel that can selectively release active compounds in microglial cells and astrocytes is developed and characterized. The degree of selectivity and subcellular distribution of the nanogel is evaluated by applying an innovative super-resolution microscopy technique, expansion microscopy. Two different administration schemes are then tested in a SCI mouse model: in an early phase, the nanogel loaded with Rolipram, an anti-inflammatory drug, achieves significant improvement in the animal's motor performance due to the increased recruitment of microglia and macrophages that are able to localize the lesion. Treatment in the late phase, however, gives opposite results, with worse motor recovery because of the widespread degeneration. These findings demonstrate that the nanovector can be selective and functional in the treatment of the glial component in different phases of SCI. They also open a new therapeutic scenario for tackling glia-mediated inflammation after neurodegenerative events in the central nervous system.

1. Introduction

Spinal cord injury (SCI) is one of the most devastating of neurological diseases. Progressive neuropathological events after the primary injury lead to further damage of the spinal cord, worsening the clinical outcome. Secondary neuropathological events contribute to progression of the injury and have important effects on neurodegeneration and SCI outcomes.[1,2] The inflammatory response plays a key role in this process, and its dynamic events include a complex variety of cells around the injured site.

Our understanding of SCI inflammation has greatly increased in recent years.[3–6] Recently single-cell analysis has been employed to investigate cell heterogeneity in the injured site.[7,8] This study revealed different microglia subpopulations based on their transcriptional profiles. Homeostatic microglia are present in uninjured mice. One day post-injury (DPI), almost all microglia cells retrieved from

V. Veneruso, E. Petillo, D. Comolli, M. De Paola, G. Forloni, P. Veglianese
Department of Neuroscience
Istituto di Ricerche Farmacologiche Mario Negri IRCCS
via Mario Negri 2, Milano 20156, Italy
E-mail: pietro.veglianese@marionegri.it

V. Veneruso, A. Verrillo, A. Baggiolini, P. Veglianese
Faculty of Biomedical Sciences
Università della Svizzera Italiana
via Buffi 13, Lugano 6900, Switzerland

The ORCID identification number(s) for the author(s) of this article can be found under https://doi.org/10.1002/adma.202307747

DOI: 10.1002/adma.202307747

F. Pizzetti, S. Votano, F. Castiglione, M. Sponchioni, F. Rossi
Department of Chemistry
Materials and Chemical Engineering "Giulio Natta"
Politecnico di Milano
via Mancinelli 7, Milano 20131, Italy

A. Orro
Department of Biomedical Sciences National Research Council
Institute for Biomedical Technologies
Via Fratelli Cervi 93, Segrate 20054, Italy

A. Verrillo, A. Baggiolini
Institute of Oncology Research (IOR)
BIOS+
Via Francesco Chiesa 5, Bellinzona 6500, Switzerland

the injury site shift toward an inflammatory and proliferative phenotype. Afterward, between 3 and 7 DPI, the inflammatory signature gradually changed toward a more activated phenotype.[7,8]

However, astrocytes are not a uniform population, but present a complex spectrum of activation states with opposing phenotypes. Some astrocytes are destructive (A1), while others are beneficial (A2).[9,10] Different types of astrocytes in the spinal cord after contusion have been identified by gene expression analysis: naive astrocytes, reactive astrocytes, and scar-forming astrocytes.[11] Six astrocyte subtypes have been demonstrated at single-cell resolution during the progression of the lesion.[12] Astrocytes also communicate functionally with microglia,[9,13] which are involved in the spread of the secondary injury. Microglia can in fact activate astrocytes by paracrine signals, inducing pro-inflammatory astrocytes.[9,13] This suggests a link between microglia and astrocyte activation that can propagate the inflammatory response and contribute to SCI.

We observed dramatic changes in the disease outcome depending on whether microglia or astrocytes were specifically targeted pharmacologically at different time points post-injury.[14,15] Different authors have demonstrated that in the later phase microglia and astrocytes work together to play a protective role, acting as a barrier in the scar tissue and reducing widespread degeneration, as suggested recently.[3–7,16–18] These results indicate a complex scenario for the glia-based inflammasome, and suggest that finely tuned therapy aimed at a single cellular target might offer a promising way to modulate the unique behavior of these cells for successful treatment.

More recent immunomodulatory therapeutic approaches have focused on attenuating the inflammation or polarizing endogenous cells toward a reparative phenotype.[19] However, a large number of pharmacological treatments have not taken account of the unique response of specific cells, and have often pursued general treatments involving many cellular components, generating some undesirable effects or not maximizing the response to the treatment.[19] Furthermore, developing effective immune-based therapies is challenging because we have no innovative strategies to target specific glial cells, and because the glial response is heterogenous and responds to multiple molecular pathways. Therefore, fine-tuned therapy aimed at cellular targets remains essential for successful treatment. Nanoparticles (NPs) are a promising tool that can be tailored to different cell targets to achieve therapeutic effects. NPs in their various forms have increasingly important roles as targeted delivery systems in the treatment of many diseases.[20,21] Their numerous advantages include better drug delivery, controlled biodistribution, and release of different compounds.[21] They also limit the potential side effects of treatment.[20,21] Strategic compounds can be delivered selectively to the specific cells considered the primary target of the treatment, and fine control of how the NPs internalize and interact with cells is important to ensure the best possible effect of the therapeutic compounds. Different NPs have been investigated, but none have shown tropism for both microglia and astrocytes of the spinal cord.

In this study, we characterize and evaluate a multi-cell therapy to target a common inflammatory pathway in microglia and astrocytes. A drug (Rolipram) will be administered in nanogel-based nanoparticles (hereafter referred to as NG) that are exclusively internalized by microglia and astrocytes in the injured spinal cord. This drug will be used to block the translocation of NFκB, which in turn reduces the production of pro-inflammatory factors and limits the negative effect of the inflammatory response after SCI.

2. Results

2.1. Synthesis and Characterization of NG

NGs were synthesized through emulsification evaporation between rhodamine-polyethyleneimine (PEI) and polyethylene glycol (PEG)-1,1′-carbonyldiimidazole (CDI, bis functionalized). After sonication, the colloidal dispersion was left to rest, to allow the evaporation of the solvent and then freeze-dried. The synthesis performed allows to obtain NGs with round shape (Figure S1A-a, Supporting Information) with mean diameter of 150 nm and polydispersity index of 0.15 (Figure S1A-b, Supporting Information) as visible from atomic force microscopy and dynamic light scattering (DLS) analyses (Figure S1A-b, Supporting Information). NGs were also analyzed using Fourier transform infrared method confirming the occurred synthesis. In particular, the carbamate group, responsible for the chemical bonds between the two polymers used could be recognized at 1620 cm^{-1} (1, asymmetric stretching COO-), 1440 cm^{-1} (2, symmetric stretching COO-), and 1290 cm^{-1} (3, N-COO- stretch) (Figure S1A-c, Supporting Information). After Rolipram loading, the dimension of the NGs was checked underlining only a small variation with respect to the neat NGs. Loaded NGs present a mean diameter of 168 nm and polydispersity index of 0.18. Then the release profile of Rolipram was studied and its cumulative release versus time is plotted in Figure S1A-d in the Supporting Information. The release rate is characterized by a burst release of around 28% then followed by a controlled Fickian diffusion.

2.2. Internalization of NG in Spinal Cord Glial Cell Cultures

To assess the internalization of NG in glial cells, we plated primary mono-cultures of astrocytes or microglia from the murine embryonic spinal cord or human iPSC-derived astrocytes or microglia. Glial cells were induced to an inflammatory state by treating them with lipopolysaccharide (LPS) for 18 h, and then they were exposed to NG for 24 h. Rhodamine B (RhB) conjugated to NG was recorded by fluorescence microscopy in microglia or astrocytes at 24 h. Murine and human glial cells were marked with CellTrace green (**Figure 1A,C**). Uptake was quantified by measuring the intensity of RhB in the cytosol of glial cells, normalized for individual cell areas identified by CellTrace green at the end of treatment. At 24 h, murine astrocytes (Figure 1A-a,b) had higher internalization of NG-RhB (Figure 1B) than microglial cells (Figure 1A-c,d). In line with murine cells, human astrocytes too (Figure 1C-a,b) had more nanovectors in astrocytes after 24 h (Figure 1D) than human microglia (Figure 1C-c,d), suggesting similar behavior in human glial cells.

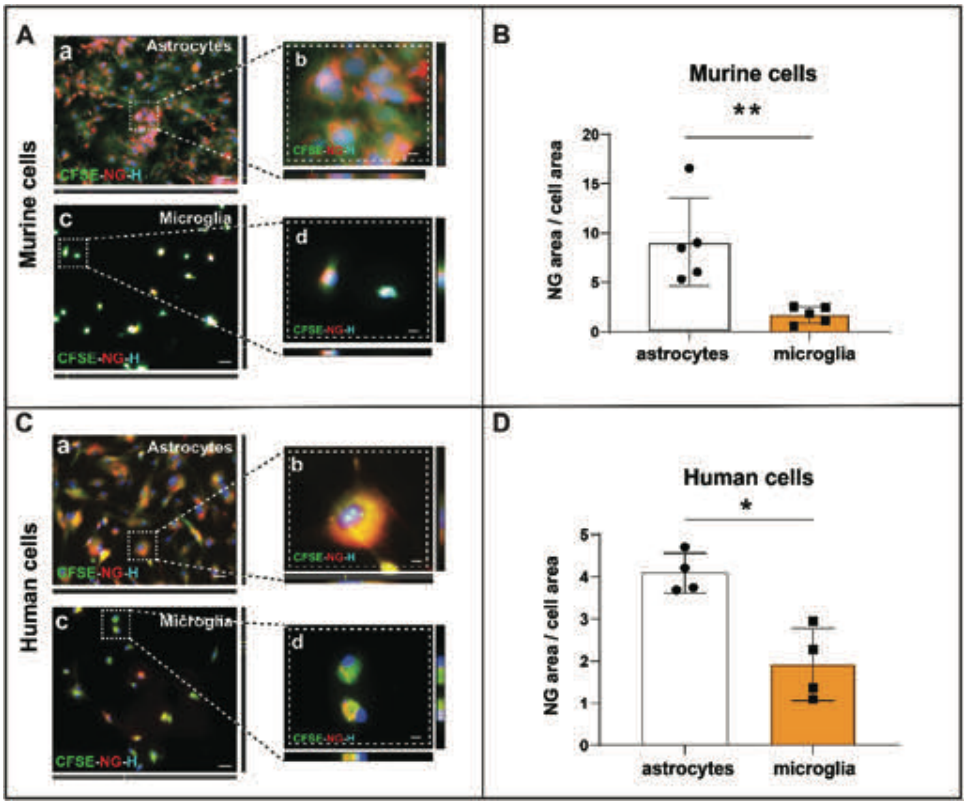

Figure 1. Characterization of NG uptake in murine or human glia culture cells. A representative image of NG internalization in A) murine and C) human glial culture cells (microglia or astrocyte cultures) is shown, recorded by fluorescence microscopy. A–D) Accumulation of fluorescent Rhodamine B conjugated to NG is shown 24 h after the treatment with NPs in both astrocytes and microglia. A a,b,B) Murine and (C a,b,D) human astrocytes accumulated more NG than (A c,d,B) murine and (C c,d,D) human microglia. Scale bar = A a: 80 µm; A b: 30 µm; A c: 80 µm; A d: 30 µm; C a: 80 µm; C b: 30 µm; C c: 80 µm; C d: 30 µm. Statistical significance was determined with the Mann–Whitney test; two-tailed. $N = 5$; 1 outlier (alpha = 0.05). Data are presented as mean ± SD. Statistical significance: (*) $p < 0.05$, (**) $p < 0.01$.

2.3. Validation of the Nanoscale Dispersion of NPs in Primary Glial Cell Cultures

Many studies have used conventional optical microscopy to investigate NP internalization at the subcellular level,[22] but concerns remain about their distribution, interaction, and colocalization with organelles and intracellular structures, because of the limited resolution achieved (about 250 nm), which is often only an approximation. In the last decade, important innovations have been introduced in optical microscopy, to overcome this limit of resolution (200–300 nm). New super-resolved techniques have been proposed in life science imaging and some techniques reach a few tens of nanometers of resolution (see review[23]). NP investigation can draw on these innovations to gain greater detail, discrimination, and accuracy at the subcellular level.

Expansion microscopy (ExM) is a recent super-resolved approach, permitting 3D nanoscale imaging of swelled specimens.[24–28] After controlled physical expansion, molecules are separated, increasing the distance between them, and overcoming the diffraction limit, to reveal finer details with a conventional microscope.[24–28] We demonstrated the ability of the ExM protocol to expand isolated NPs in vitro. NPs with different physico-chemical features were considered: FluoroSphere (FS), poly-ϵ-caprolactone (PCL)-based NPs, and PEG-PEI nanogel-based NPs (NG). FS are commercially available (Figure S1B, Supporting Information) and chemical structure is based on polystyrene NPs coated with sulfate groups. PCL (Figure S1D, Supporting Information) and NG (Figure S1F, Supporting Information) were synthesized as previously demonstrated.[14,15,29] The three nanovectors used are comparable in terms of shape (spherical), mean diameter, and polydispersity index. FS represents nondegradable hydrophobic colloidal dispersions, PCL degradable hydrophobic ones, and NG hydrophilic ones. Differently from FS and PCL, NG can adsorb water and swell to greater volume. The NPs, dispersed 2% in water (w/v) for FS, PCL, and NG, were spotted on coverslips and acquired by conventional epifluorescence microscopy (Figure S1B,D,F, Supporting Information). Their mean diameter was about 100 nm, but several clusters of NPs were identified. After microscopic analysis, we found the following dimensions: FS 113 ± 30 nm (mean diameter (md) ± standard deviation (SD)) (Figure S1B-a,b,e, Supporting Information), PCL 112 ± 40 nm (md ± SD) (Figure S1D-a,b,e, Supporting Information), and NG 100 ± 20 nm (md ± SD) (Figure S1F-a,b,e, Supporting Information). These are in line with DLS analysis presented previously.[14,15,29–31]

To investigate the re-sizing of these isolated NPs with the ExM protocol (see the Experimental Section), we added the colloidal systems of NPs directly to the monomer solution of

acrylamide, with no chemical anchor to the polymer matrix. After polymerization, the polyacrylamide polymer gels containing NPs, added at the concentration of 2.5 mg mL^{-1}, were isotropically expanded by adding deionized water. The mean diameters of NPs indicated equivalent re-sizing: FS 427 ± 142 nm (md ± SD) (Figure S1B-c–e, Supporting Information), PCL 440 ± 90 nm (md ± SD) (Figure S1D-c–e, Supporting Information), and NG 378 ± 75 nm (md ± SD) (Figure S1F-c–e, Supporting Information), and showing enlargement of all the NPs about four times their original size.

In line with the widefield microscopic analysis, scanning electron microscopy (SEM) showed that all NPs presented regular re-sizing and were spherical (Figure S1C,E,G, Supporting Information) and quantified (SmartPI software) fourfold expansion in each dimension: FS 450 ± 52 nm (md ± SD) (Figure S1C-a,b, Supporting Information), PCL 425 ± 35 nm (md ± SD) (Figure S1E-a,b, Supporting Information), and NG 405 ± 38 nm (md ± SD) (Figure S1G-a,b, Supporting Information). This suggests that the physical expansion for nanomaterial of different chemical origin is feasible and enlargement of the nanostructure quite likely results from local forces which, acting on the physical structure, follow the isotropic force imposed by the swelling of the polymer. It has been previously reported that a similar ExM protocol generates a gel with mesh size 1–2 nm, which can explain the entrapment of structures of a few hundred nanometers such as NPs.

In accordance with this, the proton NMR spectra of the swollen polymers are reported in Figure S2 in the Supporting Information. All spectra present broad peaks in the aliphatic region in the range 1.2–2.5 ppm. The methylene (–CH_2–) groups of the polymer give three peaks for each polymer repeat unit, one at 1.73 ppm from polyacrylate, two overlapping peaks from the repeat units at 1.60 and 1.55 ppm (Figure S2-b–d, Supporting Information). The methine (–CH<) groups give rise to partly resolved peaks in the range 2.1–2.5 ppm. Small peaks at 3.9–4.3 ppm are due to O-CH_2 groups, Similar features, with no marked differences, are seen in the nanoparticle-polymer spectra (Figure S2-b–d, Supporting Information) compared with the initial neat hydrogel (Figure S2a, Supporting Information). This confirms the absence of chemical bonds between gels and nanoparticles.

To demonstrate the utility of investigating NG at the subcellular level with nanoresolution, we analyzed NG in cultures of primary astrocytes. We pretreated microglia with lipopolysaccharide (LPS) and astrocytes with pro-inflammatory factors complement 1 q (C1q), tumor necrosis factors-alpha (TNF-α), and interleukin-1 (IL-1) α, in vitro for 18 h to induce cell activation.[13] We then exposed the cells to NG (2.5% w/v) for 24 h, after which the NG was removed and the sample was processed for expansion (see the Experimental Section). The sample was pretreated with glutaraldehyde to anchor the cell proteins to the polymer matrix and ensure isotropic expansion.[32] After the expansion, we checked that controlled homogenous rescaling was achieved. We examined stereotyped structures such as microtubules in astrocytic cells by imaging tubulin stained with an antitubulin antibody conjugated to CF660, comparing the samples before and after expansion (Figure S3A, Supporting Information). Astrocytes were acquired by super-resolution microscopy (structured illumination microscopy, SIM), subjected to the ExM protocol, and then acquired by widefield fluorescence microscopy. The same cells were identified in both sets of images.

To analyze the pre- (Figure S3A-a, Supporting Information) and post-ExM samples (Figure S3A-b, Supporting Information), the images were re-sized and dragged to overlap (Figure S3A-c, Supporting Information). We calculated an expansion factor of 4.076 ± 0.1245 (md ± SD). The root mean square error (RMS) of the distortion between aligned microtubules in the pre- and post-ExM images was calculated using a custom-written Mathematica routine, already published[33] (Figure S3A-d, Supporting Information). Three separate regions of the cell showed a distortion of 0.39 µm at a length scale of 15 µm, corresponding to 2.6% relative distortion (Figure S3A-e, Supporting Information).

To validate the correct location and distribution of the NPs in the expanded cells, using SIM we identified single clusters of NG in the cytosol of astrocytes and compared them to the same clusters after expansion (Figure S3B-a–c, Supporting Information). Although the pre- and post-ExM images were paired, it was hard to match some NG clusters closely because of axial expansion, which can cause objects to appear out of focus (Figure S3B-b–d, Supporting Information). The RMS of the distortion was reported to be 0.49 µm at a length of 15 µm, corresponding to 3.3% of relative distortion (Figure S3B-d,e, Supporting Information). This confirms that the NPs pattern in the cell was minimally distorted.

2.4. Nanoresolved Subcellular NG Distribution in Murine and Human Glia Cell Culture

Detailed characterization of intracellular NPs and their interactions with subcellular organelles is a challenging task due to the inadequate resolution of conventional microscopic analysis. Here, we used ExM to study the subcellular interactions of NG with cell organelles in murine and human astrocytes or microglia 1 and 24 h after exposure to the nanovector. Once internalized, NG was entrapped in endosomal vesicles of murine (**Figure 2B**) and human astrocytes (Figure 4B). Endosomes were identified by immunostaining of Early Endosome Antigen 1 (EAA1) in murine (Figure 2B-a,b) and human (Figure 4B-a,b) astrocytes and the diameter of the EAA1 fluorescence signal was calculated from the full-width at half-maximum (FWHM) of 111 nm in murine astrocytes (Figure 2B-b). The colocalization of fluorescent Rhodamine B-positive NG (red signal) with EAA1 (green signal), as measured by Pearson's coefficient, indicated partial colocalization in murine astrocytes (Figure 2B-c), suggesting that the endosomes incorporated NG. Human iPSC-derived astrocytes had even clearer rhodamine-positive nanoparticles in the early endosome, as the larger size of human astrocytes allowed for better visualization (Figure 4B-a–c).

Contrary to what was observed in other cell types, in murine and human microglia NG was internalized into the cytosol, but not entrapped in endosomal vesicles of murine (**Figure 3B-a–d**) or human microglia (Figure 5B-a–c) . In fact, the colocalization of fluorescent Rhodamine B-positive NG (red signal) with EAA1 (green signal), as measured by Pearson's coefficient, indicated no colocalization in mouse microglia (Figure 3B-d). This was confirmed in human microglia, which are larger (Figure 5B-b,c), suggesting that the endosomes did not incorporate NG.

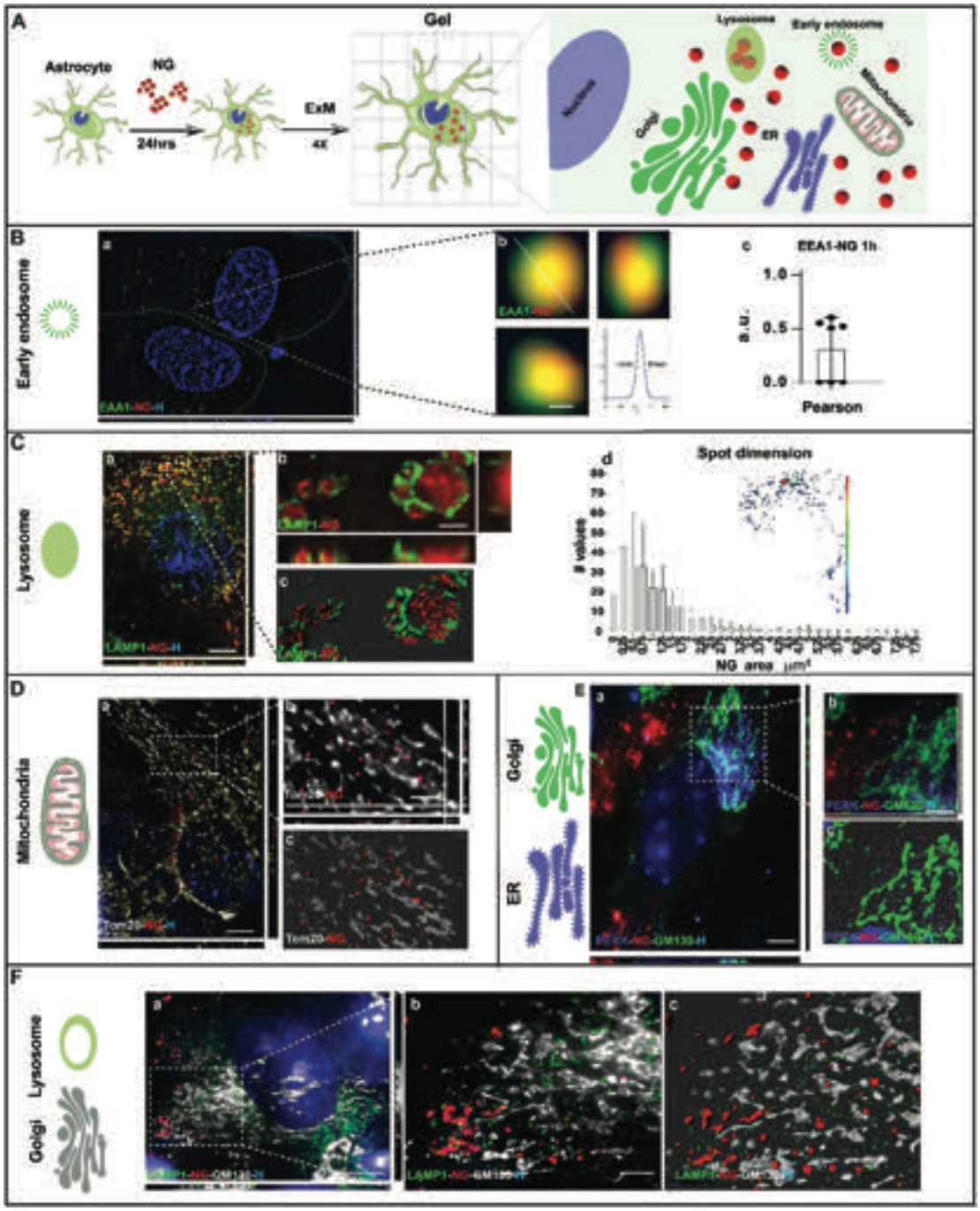

Figure 2. Super-resolved subcellular NP distribution in murine astrocyte. A) Experimental design. B) Representative image of NG (red, a,b) internalized in early endosomes (EEA1, green, a,b) distributed around the nucleus (H, blue, a) in the cytosol of astrocytes subjected to the expansion protocol. The diameter of the EEA1 fluorescence signal is calculated from the full-width at half-maximum (FWHM, b). The colocalization of the NG (red) with the EEA1 (green) signal is expressed by Pearson's coefficient with partial overlap between the signals (c). C) Representative image of the subcellular distribution of NG (red, a,b) captured in lysosomes (green, a,b) around the nucleus (H, blue, a). At 24 h from the NG exposure, astrocytes had different-sized multivesicular body lysosomes, as shown by frequency distribution analysis (d), and bigger multivesicular body lysosomes containing large amounts of NG (b–d pseudocolor inset). D) Representative image of NG (red, a,b), mitochondria, stained with TOM20 (white, a,b), and cell nuclei (H, blue, a) 24 h after nanovector exposure. NG (red) was not colocalized with mitochondria (white), as shown by isosurface reconstruction (c). E) Representative image of NG (red, a,b), endoplasmic reticulum (PERK, purple, a,b), Golgi apparatus (GM130, green, a,b), and nucleus (H, blue, a) 24 h after NG exposure. NG colocalization was not seen with ER, as shown by isosurface reconstruction (c). F) Representative images of the distribution in the cytosol of astrocytes around the Golgi apparatus (GM130, white, a,b) and nucleus (H, blue, a) of lysosomal vesicles (LAMP1, green, a,b) and NG (red). Some NG was entrapped in the Golgi cisternae (a) as shown by the magnified views of the boxed region of the image a (b) and by isosurface reconstruction (c). Scale bar = B a 1 µm; B b 50 nm; C a 1 µm; C b 0.5 µm; D a 1 µm; D b 0.5 µm; E a 1 µm; E b 0.5 µm; F a 1 µm; F b 0.5 µm. $N = 7$. Data are presented as mean ± SD.

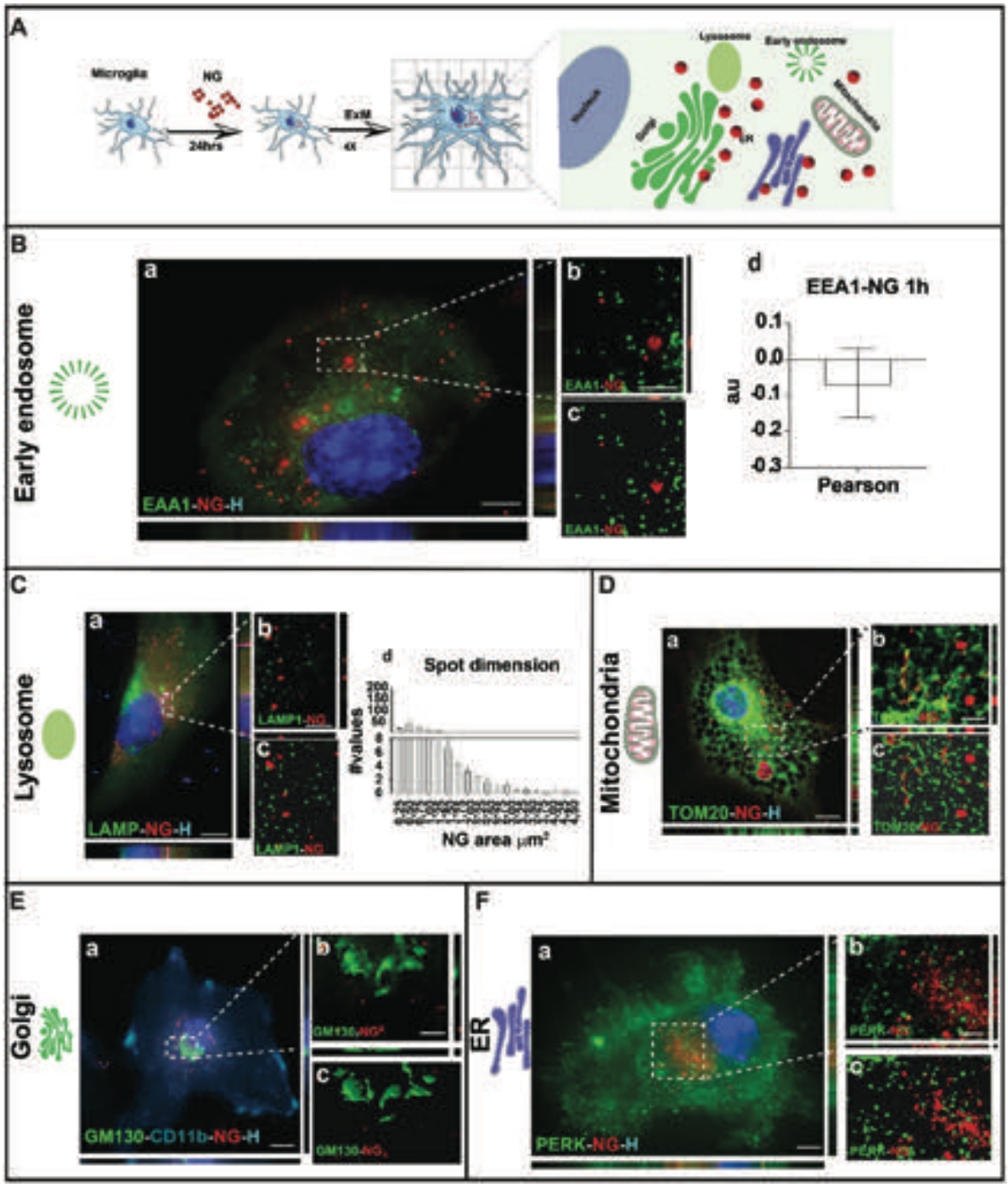

Figure 3. Super-resolved NPs distribution at subcellular level in murine microglia. A) Experimental design. B) Representative image of NG (red, a,b) not entrapped in early endosomes (EEA1, green, a,b) distributed around the nucleus (H, blue, a) in the cytosol of microglia shown after the expansion protocol (a–c). The lack of colocalization of the NG (red) with the EEA1 (green) signal is expressed by Pearson's coefficient (d). C) Representative image of the subcellular distribution of NG (red, a,b) not detected in lysosomes (LAMP1, green, a,b) distributed around the nucleus (H, blue, a). At 24 h from the NG exposure, microglia showed different-sized lysosomes (b,c), as indicated by the frequency distribution (d). D) Representative image of NG (red, a,b), mitochondria, stained with TOM20 (green a,b), and cell nuclei (H, blue, a,b) 24 h after nanovector exposure. NG (red) was not entrapped in mitochondria (green), as shown by isosurface reconstruction (c). E) Representative image of NG (red, a,b), Golgi apparatus (GM130, green, a,b), microglia staining (CD11b, cyan, a,b), and nucleus (H, blue, a) 24 h after NG exposure. Colocalization of NG and GM130 was not seen (a,b), as shown by isosurface reconstruction (c). F) Representative image of NG (red, a,b), ER, stained with PERK (green, a,b), and cell nuclei (H, blue, a) 24 h after nanovector exposure. NG (red) was not entrapped in ER (green), as shown by isosurface reconstruction (c). Scale bar = B a 1 µm; B b 0.5 µm; C a 1 µm; C b 0.5 µm; D a 1 µm; D b 0.5 µm; E a 1 µm; E b 0.5 µm; F a 1 µm; F b: 0.5 µm. $N = 11$; 1 outlier (alpha 0.05). Data (B d) are presented as mean ± SD; Data (C d) are presented as mean ± SEM.

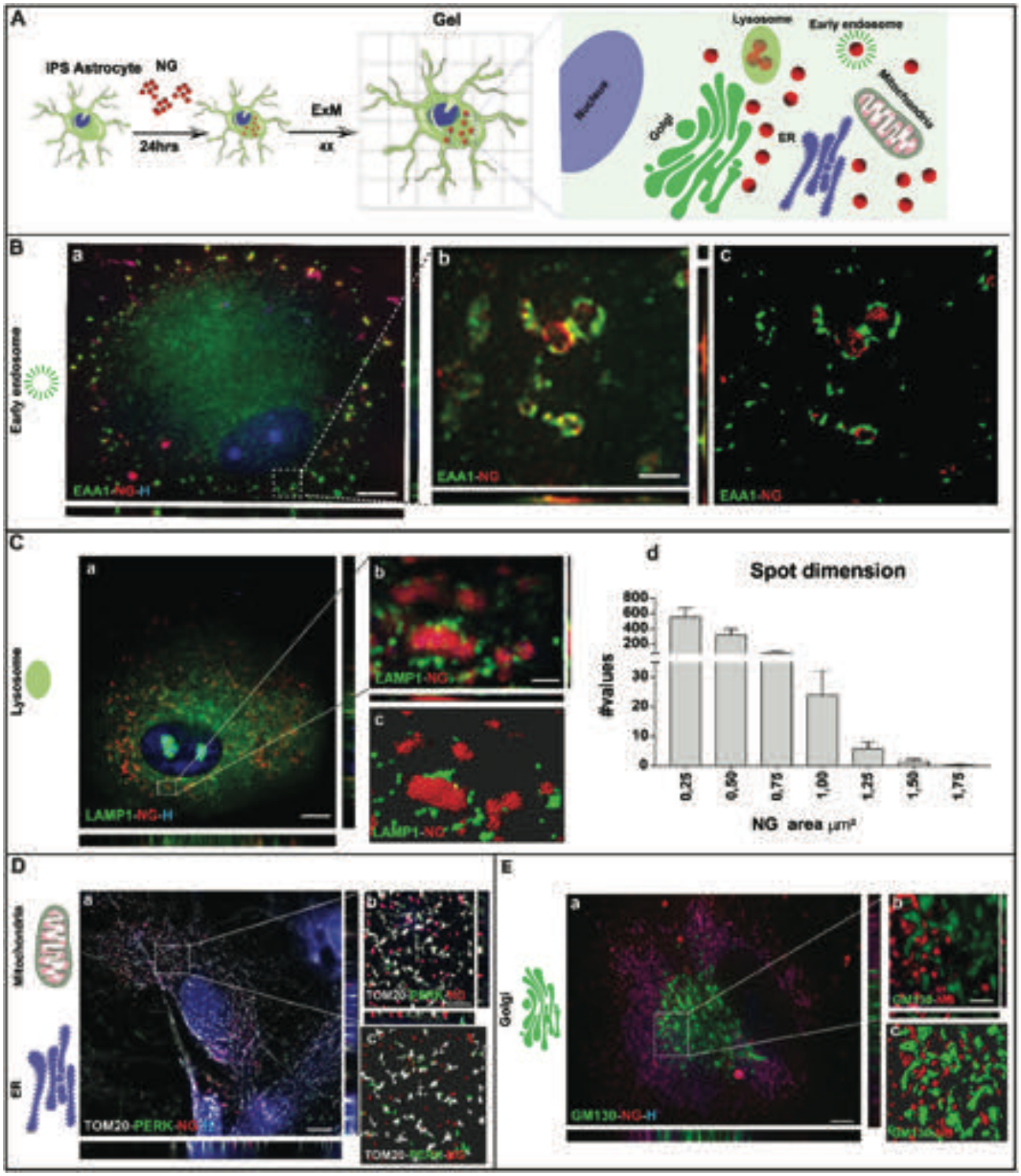

Figure 4. Super-resolved NPs distribution at subcellular level in human iPS-derived astrocytes. A) Experimental design. B) Representative image of NG (red, a,b) internalized in early endosomes (EEA1, green, a,b) distributed around the nucleus (H, blue, a) in the cytosol of human astrocytes subjected to the expansion protocol. C) Representative image of the subcellular distribution of NG (red, a,b) not captured in lysosomes (LAMP1, green, a,b) around the nucleus (H, blue, a). At 24 h from the NG exposure, astrocytes had different-sized multivesicular-body lysosomes, as shown by frequency distribution analysis (d). D) Representative image of NG (red, a,b), mitochondria, stained with TOM20 (white, a,b), PERK (green, a,b), and cell nuclei (H, blue, a) 24 h after nanovector exposure. NG (red) was not colocalized with mitochondria (white) or ER (green), as shown by isosurface reconstruction (c). E) Representative image of NG (red, a,b), Golgi apparatus (GM130, green, a,b), and nucleus (H, blue, a) 24 h after NG exposure. NG colocalization was not seen with GM130, as shown by isosurface reconstruction (c). Scale bar = B a: 0.7 µm; B b: 0.3 µm; C a: 0.7 µm; C b: 0.3 µm; D a: 0.7 µm; D b: 0.3 µm; E a: 0.7 µm; E b: 0.3 µm. Data are presented as mean ± SEM.

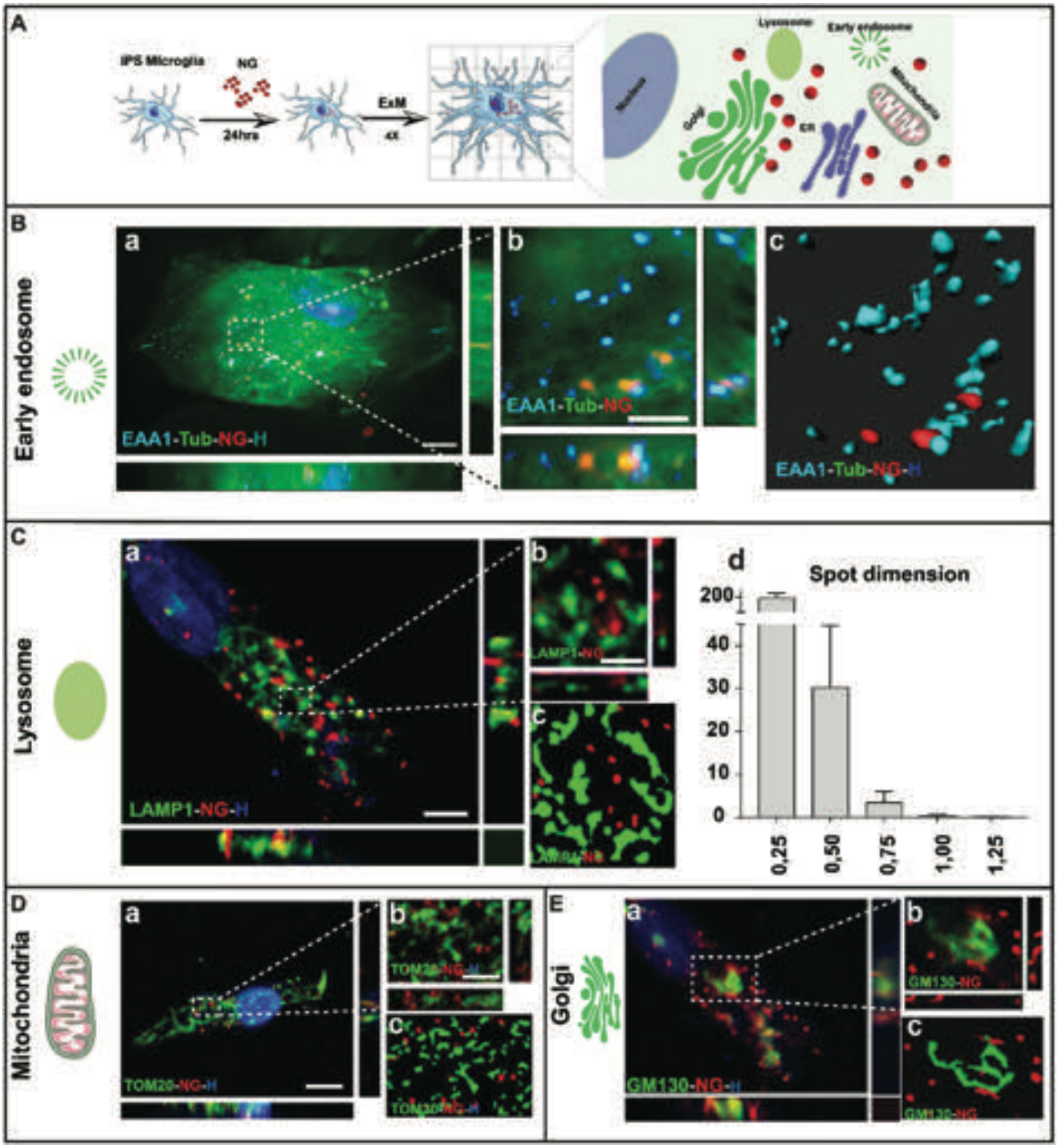

Figure 5. Super-resolved NPs distribution at subcellular level in human iPS-derived microglia. A) Experimental design. B) Representative image of NG (red, a,b) not entrapped in early endosomes (EEA1, cyan, a,b) distributed around the nucleus (H, blue, a) in the cytosol of microglia stained by tubulin (Tub, green, a,b) shown after the expansion protocol (a–c). C) Representative image of the subcellular distribution of NG (red, a,b) not detected in lysosomes (LAMP1, green, a,b) distributed around the nucleus (H, blue, a). At 24 h from the NG exposure, microglia had different-sized lysosomes (b,c), as represented by frequency distribution (d). D) Representative image of NG (red, a,b), mitochondria, stained with TOM20 (green, a,b), and cell nuclei (H, blue, a) 24 h after nanovector exposure. NG (red) was not entrapped in mitochondria (green), as shown by isosurface reconstruction (c). E) Representative image of NG (red, a,b), Golgi apparatus (GM130, green, a,b), and nucleus (H, blue, a) 24 h after NG exposure. Colocalization of NG and GM130 was not seen (a,b), as shown by isosurface reconstruction (c). Scale bar = B a 0.7 μm; B b 0.3 μm; C a 0.7 μm; C b 0.3 μm; D a 0.7 μm; D b 0.3 μm; E a 0.7 μm; E b 0.3 μm. Data are presented as mean ± SEM.

After 24 h, NG was redistributed in the perinuclear region of the murine (Figure 2C-a–c) and human astrocytes (**Figure** 4C-a–c), associated with lysosomal vesicles. These were marked with antilysosomal-associated membrane protein 1 (anti-LAMP1), clearly distributed in the membrane of the murine (Figure 2C-a–c) and human (Figure 4C-a–c) lysosomes. NG was captured in the lysosomes at 24 h and vesicles had different sizes in both murine (Figure 2C-d) and human astrocytes (Figure 4C-d), probably due to the fusion for the formation of hybrid lysosome organelles.

Contrary to what was observed in astrocytes, they were not found to be entrapped in lysosomal vesicles of murine (Figure 3C) or human microglia (**Figure** 5C) suggesting an alternative degradative pathway in microglial cells.

To investigate the impact of NG on the Golgi apparatus, we stained the network with an anti-GM130 antibody directed to the cytoplasmic protein that is bound to cis-Golgi membranes. The Golgi apparatus is the most important organelle involved in protein and lipid modifications, and conventional microscopy, which can only resolve structures about 200 nm in size, limits the examination of Golgi cisternae (<100 nm). To overcome this limit, we used ExM to see the interactions between NG and Golgi structures. GM130 staining indicated that in untreated astrocytes, the Golgi apparatus had regular, normal ribbon-like structures (Figure S4A-a,b, Supporting Information). Murine (Figure 2E,F and Figure S4A, Supporting Information) or human (Figure 4E and Figure S4B, Supporting Information) astrocytes exposed to NG for 24 h had clusters of NG around the cisternae, but this did not modify the general Golgi structure. However, a small number of murine astrocytes (about 9–10%) had smaller cisternae and a more perinuclear location of the ribbon-like structure (Figure S4A-f, Supporting Information). There were also a few NG interspersed among the cisternae (Figure 2E,F), but the largest amount was in the cytosol, out of the Golgi apparatus.

Murine (Figure 3E and Figure S4C, Supporting Information) or human microglia (Figure 5E and Figure S4D, Supporting Information) showed no significant alterations of the Golgi apparatus, as demonstrated by quantitative analysis (Figure S4C-f,D-f, Supporting Information).

Mitochondria, identified as TOM20-positive organelles, were evenly distributed in the cytoplasm of untreated murine (Figure 2D) and human astrocytes (Figure 4D). After 24 h, astrocytes showed no evident overlap of mitochondria with NG in either murine (Figure 2D-a–c) or human astrocytes (Figure 4D-a–c). However, there was a significant increase in the branch length of mitochondria in human astrocytes (Figure S5B-f, Supporting Information), but not in the number of mitochondrial network branches (Figure S5B-e, Supporting Information). We did not find any significant differences between untreated (Figure S5A-a,b,e,f, Supporting Information) and NG-treated murine astrocytes (Figure S5A-c–f, Supporting Information).

TOM20 staining showed evident vacuolation in murine (Figure 3D-a–c) or human microglia (Figure 5D-a–c), which is common after LPS treatment.[34] This vacuolation made it difficult to quantify any interactions between NG and mitochondria.

To analyze the endoplasmic reticulum ER in astrocytes exposed to NG, we marked ER with the protein kinase R-like endoplasmic reticulum kinase (PERK) antibody. Murine astrocytes (Figure 2E and Figure S6A-a,b, Supporting Information) or microglia (Figure 3F and Figure S6B-a,b, Supporting Information) gave a cross-striated distribution signal in the perinuclear region. At 24 h from the NG exposure, the number of PERK spots was significantly greater in NG-treated murine astrocytes (Figure S6A-c–e, Supporting Information) than in the untreated astrocytes (Figure S6A-a,b,e, Supporting Information). We did not find significant differences comparing untreated (Figure S6B-a,b,e, Supporting Information) and NG-treated murine microglia (Figure S6B-c–e, Supporting Information). PERK staining did not show any clear and analyzable signal in human microglia and astrocytes, so we give just a qualitative image of the PERK distribution of iPS-derived astrocytes 24 h from the NG exposure (Figure 4D).

2.5. Subcellular NP Distribution in Nanoresolved Spinal Cord Tissue

To validate how well NG was internalized in the cytosol of microglia/macrophages and astrocytes in vivo, we injected a suspension of NG and LPS (to activate glial cells) into a hemisection of spinal cord parenchyma over a longitudinal distance of about 3 mm. 3 days later, we harvested the tissue and analyzed the distribution and internalization of the NG after rescaling the tissue by the expansion protocol (see the Experimental Section). Expanded spinal cord sections had an expansion factor of 4.38 ± 0.27 (mean expansion ± SD) (Figure S7A-b,c, Supporting Information). To establish whether it was controlled rescaling, we tested the fluorescence signal pattern of yellow fluorescent protein (YFP) positive axons of transgenic mice expressing under Thy-1 promoter in neuronal cells (Thy-1 YFP)[35] (Figure S8, Supporting Information). Spinal cord sections were acquired by widefield microscopy then subjected to the ExM protocol identifying the same axons. To analyze the same portion of tissue before and after expansion, images were re-sized and dragged to overlap. The geometry of the neuronal processes showed regular spatial expansion, confirmed by measuring the distortions with a custom-written Mathematica routine, previously published.[33] The RMS showed a distortion of 0.77 µm at 15 µm length scale, corresponding to 5.1% of relative distortion (Figure S8f,g, Supporting Information), showing the minimal distortion of the Thy-1 YFP positive filaments in the spinal cord tissue (Figure S8a–g, Supporting Information).

To examine the distribution and internalization of NG in the expanded spinal cord sections, we identified microglia/macrophages with an antibody against CD11b and stained astrocytes with an antibody against glial fibrillary acidic protein (GFAP). Early activated microglia (Figure S7B-a,b, Supporting Information) and hypertrophic astrocytes (Figure S7B-c,d, Supporting Information) were detected at the injection sites in the spinal cord. Around the injection site, NG was mostly taken up by microglia and astrocytes, as shown by the overlapping signals of RhB (NG) and CD11b (microglia) (Figure S7B-a,b, Supporting Information) or GFAP (astrocytes) (Figure S7B-c,d, Supporting Information) . These results confirmed the previous in vitro findings, demonstrating the uptake and subcellular distribution of NG in activated microglia and astrocytes in an in vivo model.

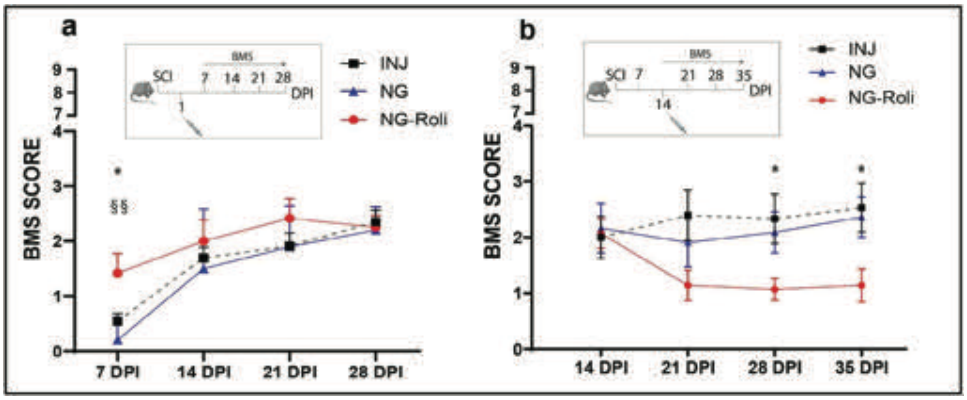

Figure 6. NG loaded with Rolipram injected 1 DPI, but not on 14 DPI, improved locomotor performance in SCI mice: A) Injection of NG loaded with Rolipram in SCI mice on 1 DPI resulted in a significant improvement of locomotor performance compared to the untreated (INJ) or NG-only (NG) groups examined on 7 DPI. B) Injection of NG loaded with Rolipram in SCI mice on 14 DPI resulted in significant impairment of locomotor performance compared to the INJ or NG group examined at 28 and 35 DPI. SCI mice were examined weekly and rated on the BMS, a scale that measures locomotor function in mice. The BMS score ranges from 0 (complete paralysis) to 9 (complete mobility, compared to healthy mice). Statistical significance was determined using one-way ANOVA followed by Bonferroni's post hoc test; two-tailed. $N = 15$ mice/group. Data are presented as mean ± SEM. Statistical significance: (*) $p < 0.05$, (§§) $p < 0.01$.

2.6. Functional Recovery Improved after an Early Treatment with NG-Roli, but without a Long-Lasting Effect SCI In Vivo

To evaluate the efficacy of a pharmacological treatment administered by NG at two different times (1 DPI or 14 DPI), we assessed the motor behavior of a mouse model of SCI in three experimental groups: an injured group, a group that received NG (NG), and a group that received NG loaded with Rolipram (NG-Roli). Nanocarriers were given through six injections with a glass capillary into the spinal cord parenchyma at 1 or 14 DPI, as previously described.[14,15] Motor recovery was assessed weekly using the Basso mouse scale (BMS) up to 35 DPI. The injured group showed partial motor recovery of the hind limbs up to 28 DPI. The NG-Roli group that received NG at 1 DPI showed significant improvement compared to the injured group at 7 DPI (**Figure 6a**), suggesting that the nanocarrier released the drug and improved motor performance, albeit not in a lasting manner. When NG-Roli was injected on 14 DPI (Figure 6b), there was no therapeutic advantage, and in fact, motor performance was significantly worse at 28 and 35 DPI. This suggests that this treatment is more effective when started in the early subacute phase rather than the subacute phase (Figure 6).

2.7. NG-Roli Acted on Early Activated Glial Cells, Reducing TNFα and Increasing CCL2 Expression in Microglia, and Reducing LCN2 Expression in Astrocytes

To demonstrate the pharmacological activity of the drug-loaded nanovector, we examined LPS-activated microglial cells that had been treated with NG-Roli. This in vitro model of early microglial activation with LPS for 24 h showed significant differences in TNFα levels when microglia were treated with NG-Roli compared to the untreated sample (Figure S9a, Supporting Information), suggesting an anti-inflammatory effect. We also observed an increase of chemokine (C—C motif) ligand 2 (CCL2) levels, a key factor for the recruitment of macrophages and other immunomodulatory cells (Figure S9b, Supporting Information). Consistent with this anti-inflammatory effect, astrocytes exposed to NG-Roli had reduced expression of the LCN2 (Lipocalin2) transcript (Figure S9c, Supporting Information). These results suggest that NG-Roli can effectively deliver Rolipram to microglia or astrocytes, thereby exploiting its pharmacological effects to reduce their early inflammatory response in a short time.

2.8. Acute NG-Roli Treatment Increased the Migration of Microglia and Macrophages in the Rostral and Caudal Regions around the Damaged Spinal Cord Site, but Did Not Alter Astrocytosis in SCI Mice

To investigate the effect of Rolipram delivered by NG at the acute stage, the NG were injected into the damaged spinal cord on 1 DPI and ex vivo tissue was analyzed after 7 DPI. Resident microglia and recruited macrophages were identified by CD11b antibody (**Figure 7**B-a,e, Supporting Information) and astrocytes by GFAP antibody (**Figure 8**B-a,e, Supporting Information) in sagittal sections of spinal cord, and the distribution, morphology, and degree of cell activation were evaluated in a rostral-caudal damaged tract of about 2.8 mm. We explored microglia, macrophages, and astrocytes phenotypes at single-cell resolution, preserving cellular spatial relationships with neuropathological lesions by a quantitative imaging pipeline powered by machine learning (see the Experimental Section). We trained microglial cells in uninjured and injured spinal cord tissue on 7 DPI to obtain a range of microglial morphological phenotypes. After prediction by machine learning (Figure 7B-b,f, Supporting Information) and the identification of single cells with different cell shape metrics (features) (Figure 7A-a,b, Supporting Information), cell area, cell perimeter, cell solidity, cell circularity, convex hull area, and convex hull perimeter were explored and processed by cluster analysis to identify three different morphological signatures: ramified, ameboid, and phagocytic-like microglia (Figure 7A-a, Supporting Information). Morphometric analysis of microglia/macrophages

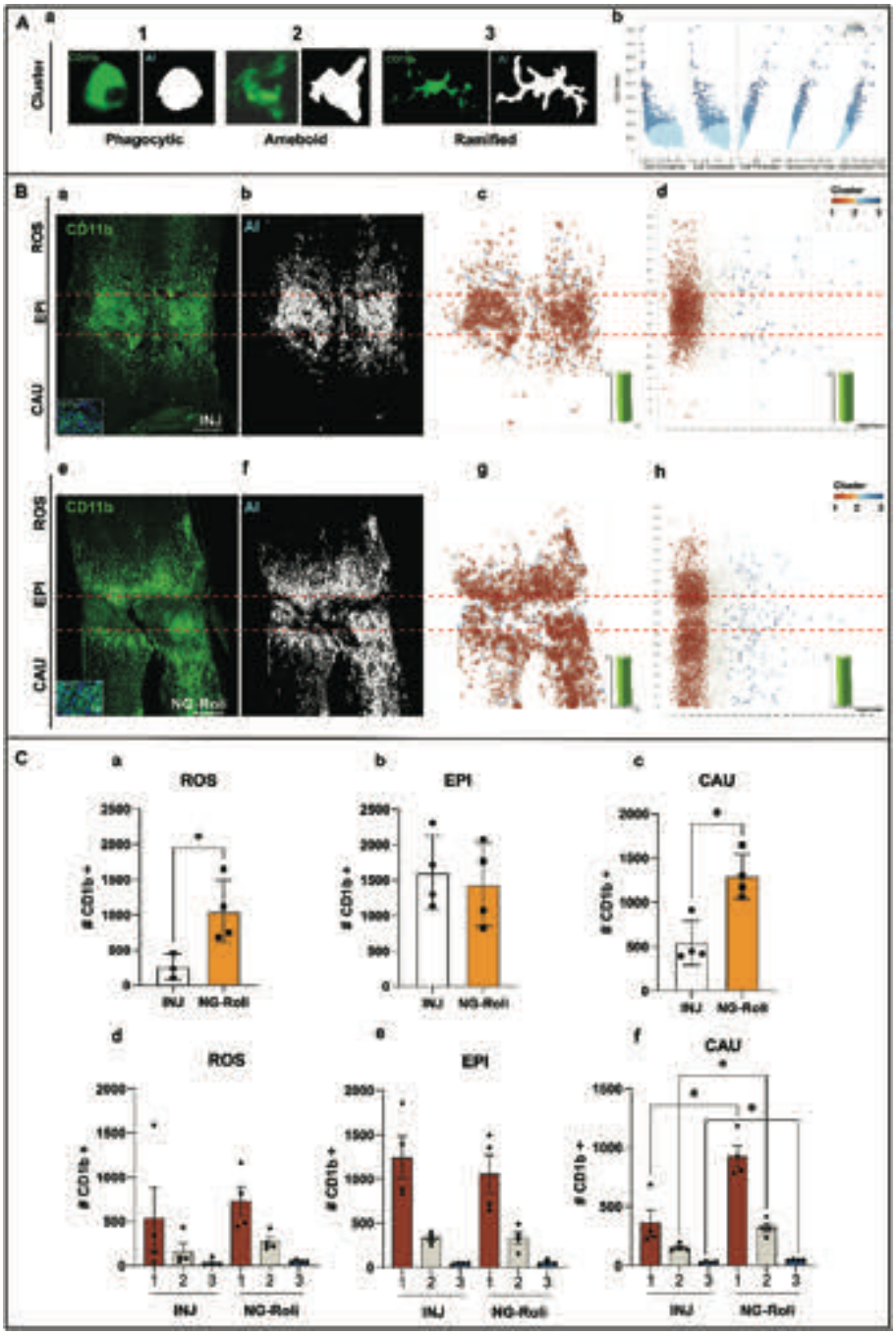

Figure 7. Classification of the morphological phenotypes of microglia or macrophages in the rostral, epicenter, and caudal tract of transversal section of spinal cord at 7 DPI after an early treatment (1 DPI). A) Representative images of different cell shape metrics to identify three different morphological cell signatures: ramified, ameboid, and phagocytic like microglia/macrophages (a). Different features were processed by cluster analysis: cell area, cell perimeter, cell solidity, cell circularity, convex hoax area, and convex hoax perimeter (b). B) Representative images of a sagittal section of spinal cord of an untreated animal stained with CD11b antibody (a; CD11b, green/Hoechst, blue inset) compared to NG-Roli treated animals (e; CD11b, green/Hoechst, blue inset). Prediction by machine learning is shown for a transversal spinal cord section of untreated (b, artificial intelligence, AI) or NG-Roli-treated animals (f, AI). Cluster analysis is shown for a transversal spinal cord section of untreated (c) or NG-Roli-treated animals (g). Cluster analysis is shown as the distribution of the single cell area (*x* axis) for a transversal spinal cord section (*y* axis) codified by cluster membership (*x* axis) of an untreated (d) or NG-Roli-treated animal (h). C) Quantitative evaluation of the total number of cells identified by machine learning showed a significant increase of cells in the rostral (a) and caudal (c) part of the lesion, but not in the epicenter (b) of the sagittal sections. Cluster analysis showed a significant increase of the phagocytic-like phenotype (f, cluster 1), ameboid (f, cluster 2), and ramified (f, cluster 3) of the microglia/macrophages in the caudal part of the lesion, but no significant differences in the rostral part (d) and epicenter (e). Statistical significance was determined using Mann–Whitney test (a–c) and Kruskal–Wallis (d–f); two-tailed. $N = 4$; 1 outlier (alpha = 0.05). Data are presented as mean ± SEM. Statistical significance: (*) $p < 0.05$; Scale bar = 250 µm.

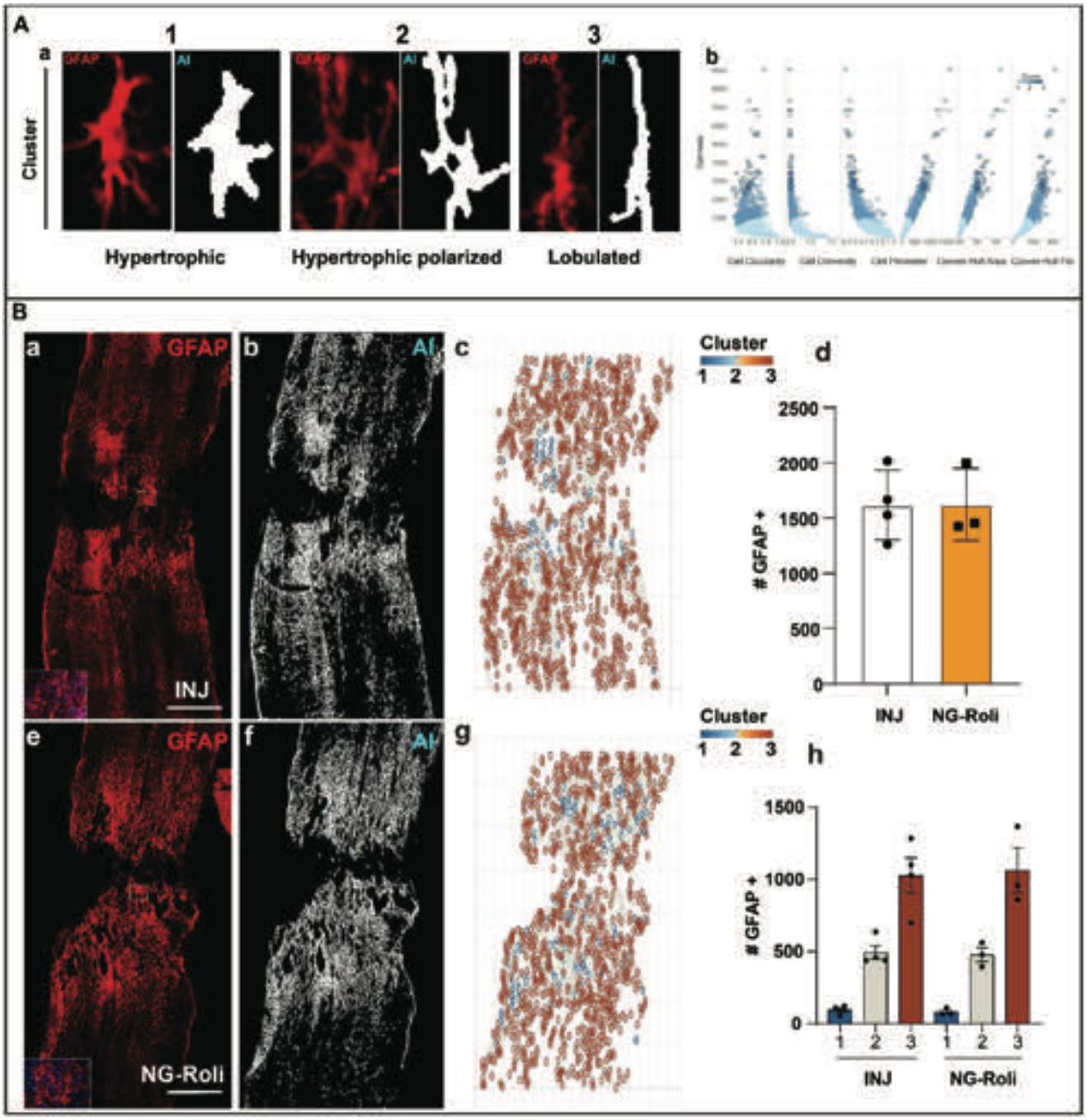

Figure 8. Classification of the morphological phenotypes of astrocytes around the epicenter of the lesion section of the sagittal spinal cord 7 DPI after early treatment (1DPI). A) Representative images of different cell shape metrics to identify three different morphological cell signatures: hypertrophic, hypertrophic polarized, and lobulated astrocytes (a). Different features were processed by cluster analysis: cell area, cell perimeter, cell solidity, cell circularity, convex hoax area, and convex hoax perimeter (b). B) Representative images of a sagittal section of spinal cord stained with GFAP antibody of untreated animals (a; GFAP, red/Hoechst, blue inset) compared to NG-Roli-treated animals (e, GFAP, red/Hoechst, blue inset). Prediction by machine learning is shown for a transversal spinal cord section of untreated (b, AI) or NG-Roli-treated animals (f, AI). Cluster analysis is shown for a transversal spinal cord section of untreated (c) or NG-Roli-treated animals (g). Quantitative evaluation of the total astrocytes identified by machine learning showed no differences in the number of cells around the epicenter of the lesion (d). Cluster analysis confirmed no differences for the hypertrophic (h, cluster 1), hypertrophic polarized astrocytes (h, cluster 2), or lobulated phenotypes (h, cluster 3). Scale bar = 250 µm. Statistical significance was determined using Mann–Whitney (d) and Kruskal–Wallis test (h); two-tailed. $N = 4$; 1 outlier (alpha = 0.05). $N = 4$. Data are presented as mean ± SEM.

during the progression of activation showed a tight correlation between some metrics: cell area of the CD11b-positive cells during the activation correlated negatively with cell solidity, cell convexity, and cell circularity, but positively with cell perimeter, cell convex hull area, and convex hull perimeter, as shown by the regression line correlation (Figure S11, Supporting Information). For cluster analysis, we took to account of the previously described metrics, and unsupervised K-means clustering was done with a predefined number of clusters parametrized with the expected morphology types, identifying at least three distinct clusters of microglia and macrophages, which we termed *phagocytic-like* (cluster 1), *ameboid* (cluster 2), and *ramified* (cluster 3). Cluster 1 was clearly the predominant cell type in the highly damaged area, with round phenotypes and greater solidity, circularity, and convexity in untreated injured mice (Figure 7B-c,d and Figure S11, Supporting Information). Ameboid cells had a larger area than phagocytic-like cells, with higher cell perimeters, cell convex hull area, and convex hull perimeter, but lower cell solidity, cell convexity, and cell circularity (cluster 2). Fewer cells were found for the morphotype identified as cluster 3, formed by a more ramified cell with reduced cell solidity, circularity, and convexity and larger cell area, perimeter, convex hull area, and convex hull perimeter than clusters 1 and 2 (Figure 7B and Figure S11, Supporting Information). Comparing spinal cord tissue of the NG-Roli group (Figure 7B-g,h) with the untreated INJ group (Figure 7B-c,d), a markedly larger amount of microglia and macrophages was found in the rostral and caudal regions of the damaged spinal cord (Figure 7B-e–h), as quantitatively shown as the total number of cells (Figure 7C-a–c). Cluster analysis also showed a significant increase of the phagocytic (cluster 1), ameboid (cluster 2), and ramified (cluster 3) morphotype in the caudal region (Figure 7C-f), and an increase was also found—but not significant—in the rostral region (Figure 7C-d). No difference was found in the epicenter tract of NG-Roli SCI animals compared to untreated injured mice (Figure 7C-b,e). In response to injury, astrocytes became reactive, followed by notable changes in morphology, including significant hypertrophy and altered ramification. An important role of astrogliosis is the confinement of the damaged area after SCI with a compact number of astrocytes surrounding the lesion, though on the other side this may be a barrier to regeneration. Severe injury of the spinal cord leads to significant cell body hypertrophy associated with the polarized elongation of distant processes toward the injury site. Similarly to microglia, we studied the activation and distribution of astrocytes in a rostral-caudal damaged tract of about 2.4 mm comparing spinal cord sagittal sections from untreated groups of animals and NG-Roli treated groups of animals stained with GFAP (Figure 8B-a,e). We trained a machine learning algorithm with astrocyte cells manually identified in uninjured spinal cord tissue and injured tissue on 7 DPI to create a set of different astrocyte morphological phenotypes. The machine learning algorithm predicted and identified single astrocytes and recorded different cell shape metrics, including cell area, cell perimeter, cell solidity, cell circularity, convex hull area, and convex hull perimeter. These metrics were then processed by cluster analysis to identify three separate morphological signatures (Figure 8A and Figure S12, Supporting Information): *hypertrophic astrocytes* (cluster 1), *hypertrophic polarized astrocytes* (cluster 2), and *lobulated astrocytes* (cluster 3). Correlation analysis of the morphometric features showed a negative pattern between cell area and cell solidity, cell convexity, and cell circularity during the different phases of activation. However, cell area correlated positively with cell perimeter, cell convex hull area, and convex hull perimeter. These results are shown in Figure S12 in the Supporting Information. The astrocyte distribution in the lesion site showed intense staining in the area around the injury, suggesting extreme activation of these cells at the epicenter of the lesion (Figure 8B-a,b). No significant differences in the total number of astrocytes were found in the sagittal sections of the spinal cord after NG-Roli treatment at the subacute SCI stage (Figure 8B-g,d) compared to the untreated group of animals (Figure 8B-c,d). A deeper assessment confirmed these results, showing no significant differences between hypertrophic (cluster 1) (Figure 8B-h), hypertrophic polarized (cluster 2) (Figure 8B-h), and lobulated astrocytes (cluster 3) (Figure 8B-h) in the sagittal sections of animals treated with NG-Roli compared to untreated groups.

2.9. Chronic NG-Roli Treatment Reduced the Number of Microglia/Macrophages in the Epicenter and Rostral Part of the Lesion in SCI Mice, but Did Not Modify Astrocytosis

To examine the effect of Rolipram delivered by NG at the transition between the subacute and chronic stage, the damaged spinal cord was injected on 14 DPI and ex vivo tissue was analyzed 30 DPI. Morphometric analysis powered by machine learning was used, and comparing spinal cord tissue of the NG-Roli group (**Figure 9**A-e,f) with the untreated INJ group (Figure 9A-a,b), there was a much smaller amount of microglia and macrophages in the rostral and epicenter regions of the damaged spinal cord, as quantitatively shown by the total number of recorded cells (Figure 9B-a,b). However, there was no significant difference in the caudal region (Figure 9B-c). In line with these findings, cluster analysis showed a significant reduction of the phagocytic morphotype (cluster 1) in the rostral (Figure 9B-d) and epicenter tracts (Figure 9B-e) of NG-Roli SCI animals compared to untreated injured mice. Comparing the total number of astrocytes after an automatic count implemented by machine learning, no significant differences were found in the sagittal sections of the spinal cord after NG-Roli treatment in the chronic SCI stage group (**Figure 10**e–h) compared to the untreated group of animals (Figure 10a–d). Cluster analysis did not show any differences (Figure 10h).

3. Discussion

Growing evidence indicates that glial cells might be a therapeutic target in SCI.[20–23] However, to date the main therapeutic challenge is how to effectively modulate these cells, taking into account specific therapeutic windows after SCI. Engineered NPs have been widely developed for diagnostic and therapeutic use in the last decade.[36–39] In this study, we demonstrate that NG-structured NPs can be specifically internalized by microglia and astrocytes, where they can release drugs (Rolipram) and act on the glial inflammatory response.

To understand their interactions at subcellular level better, we used an innovative microscopic technique called ExM. The

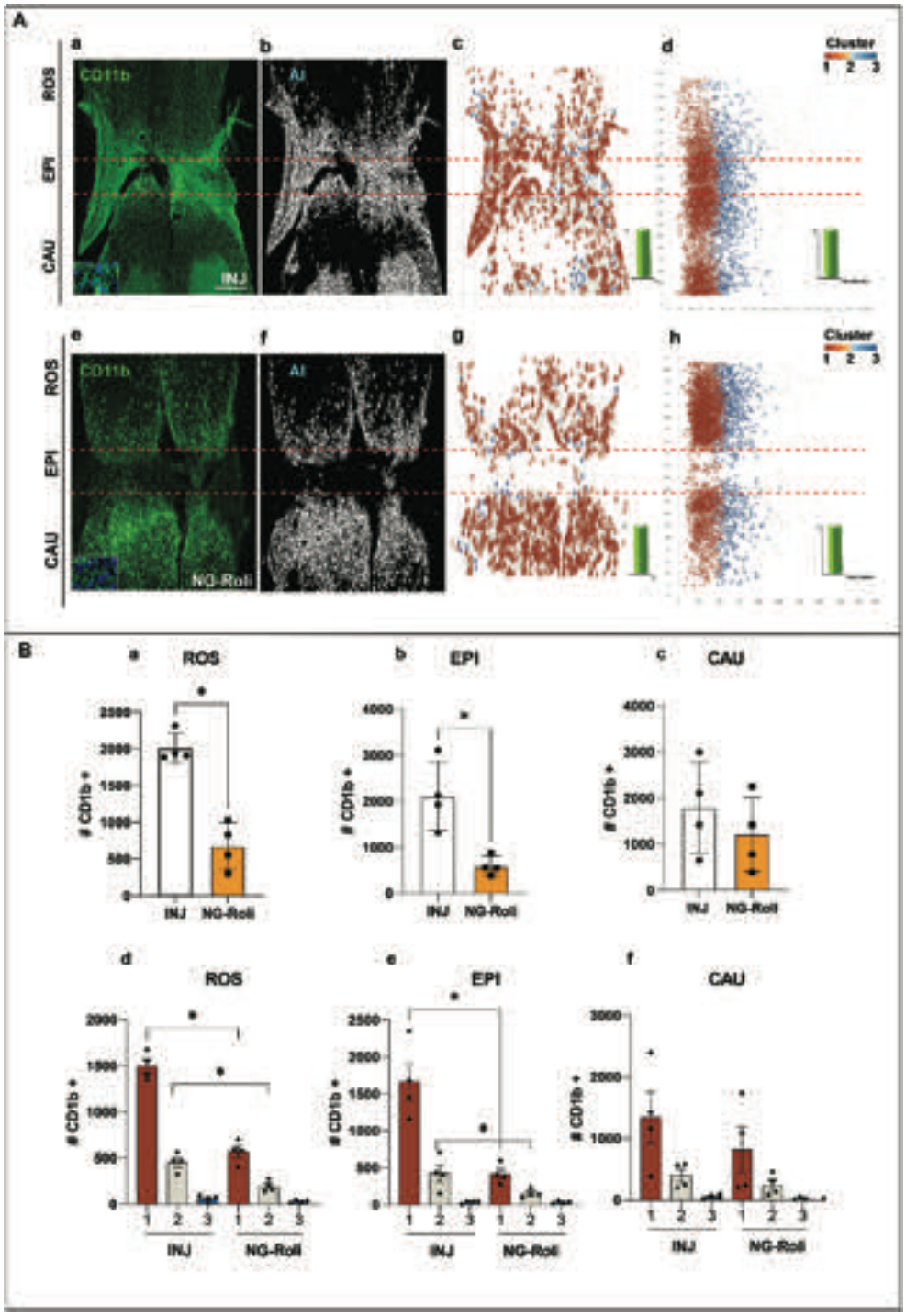

Figure 9. Classification of the morphological phenotypes of microglia or macrophages in the rostral, epicenter, and caudal tracts of the transversal section of spinal cord 35 DPI after late treatment (14 DPI). A) Representative images of a sagittal section of spinal cord stained with CD11b antibody of untreated animals (a; CD11b, green/Hoechst, blue inset) compared to NG-Roli-treated animals (e; CD11b, green/Hoechst, blue inset). Prediction by machine learning is shown for a transversal spinal cord section of untreated (b, AI) or NG-Roli-treated animals (f, AI). Cluster analysis is shown for a transversal spinal cord section of untreated (c) or NG-Roli-treated animals (g). Cluster analysis is shown as the distribution of the single cell area (*x* axis) for a transversal spinal cord section (*y* axis) codified by cluster membership (*x* axis) as untreated (d) or NG-Roli-treated (h). B) Quantitative evaluation of the total number of cells identified by machine learning showed a significant reduction of cells in the rostral (a) and epicenter regions of the lesion (b), but not in the caudal (c) part of the sagittal sections. Cluster analysis showed a significant reduction of the phagocytic-like (cluster 1) and ameboid (cluster 2) of the microglia/macrophages in the rostral (d) and epicenter (e) tracts of the lesion, but not the caudal region (f). Scale bar 250 µm. Statistical significance was determined using Mann–Whitney (a–c) and Kruskal–Wallis test (d–f); two-tailed. $N = 4$; 1 outlier (alpha = 0.05). Data are presented as mean ± SEM. Statistical significance: (*) $p < 0.05$.

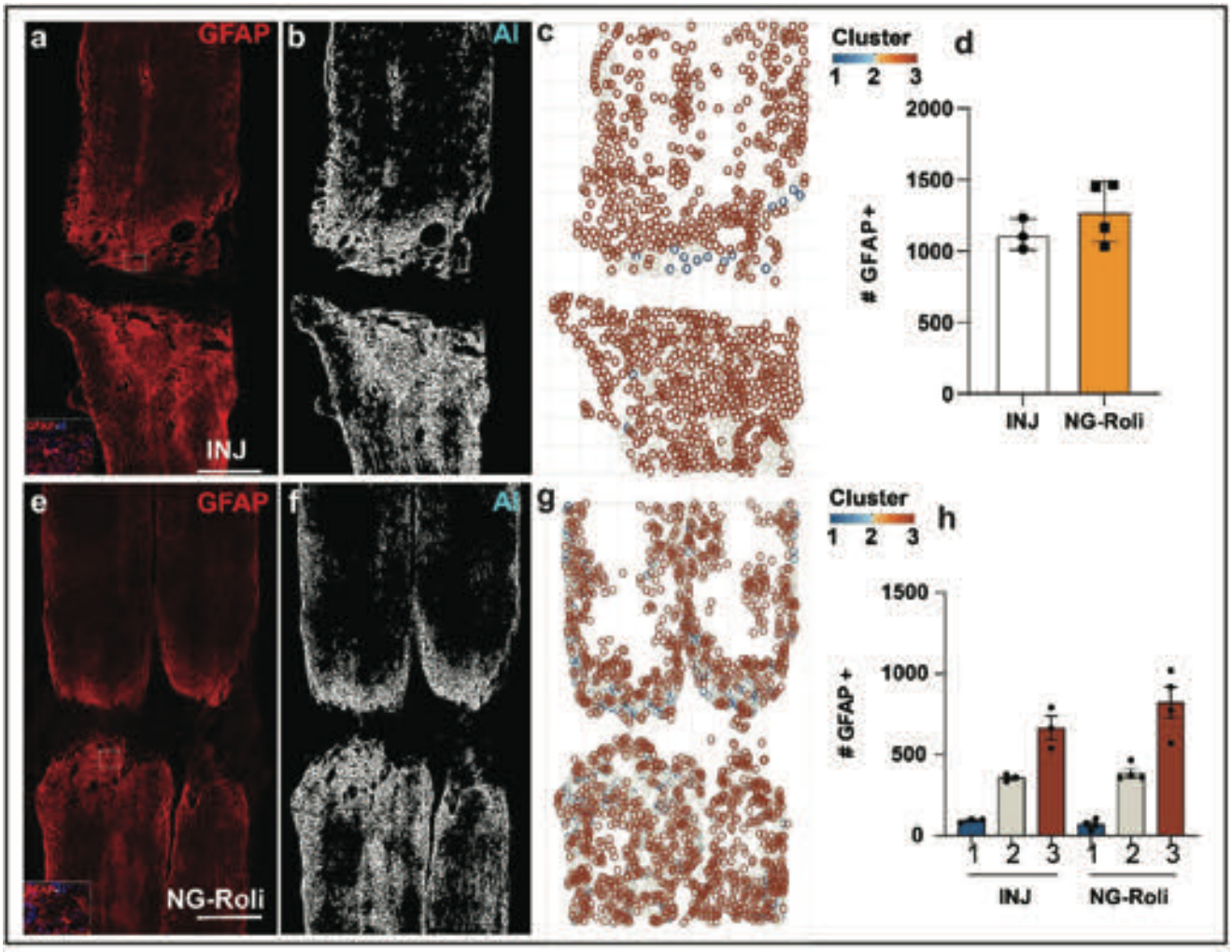

Figure 10. Classification of the morphological phenotypes of astrocytes around the epicenter of the lesion section of the sagittal spinal cord 35 DPI after late treatment (14 DPI). Representative images of a sagittal section of spinal cord stained with GFAP antibody of untreated animals (a; GFAP, red/Hoechst, blue inset) compared to NG-Roli-treated animals (e; GFAP, red/Hoechst, blue inset). Prediction by machine learning is shown for a transversal spinal cord section of untreated (b, AI) or NG-Roli-treated animals (f, AI). Cluster analysis is shown for a transversal spinal cord section of untreated (c) or NG-Roli-treated animal (g). Quantitative evaluation of the total astrocytes identified by machine learning showed no differences in the amount of cells around the epicenter of the lesion (d). Cluster analysis confirmed no differences for the hypertrophic (h, cluster 1), hypertrophic polarized astrocytes (h, cluster 2), and lobulated phenotypes (h, cluster 3). Scale bar 250 µm. Statistical significance was determined using Mann–Whitney (d) and Kruskal–Wallis test (h); two-tailed. $N = 4$; 1 outlier (alpha = 0.05). Data are presented as mean ± SEM.

nanometric dimension (1–100 nm) of NPs makes it difficult to identify and localize nanovectors in biological samples with conventional microscopy, and ExM is a promising approach to overcome this limit and allows super-resolution imaging of NPs at the subcellular level using standard fluorescence microscopes. So far ExM has been used to investigate the distribution of resized proteins,[24–28] as well as lipids,[40] glycans, small molecules, and nucleic acids.[38] We used this cutting-edge microscopic technique for the first time to detect and quantify NPs at the subcellular level, with a resolution of 70–80 nm in vitro and in vivo. The distribution of NPs in different cellular compartments, namely, endosomes, lysosomes, Golgi apparatus, endoplasmic reticulum (ER), mitochondria, and nucleus, was investigated to gain insights into their potential interactions and biological effects. After gel swelling, the NPs gave a fluorescence signal with a mean diameter of about 400 nm, suggesting that fourfold enlargement was feasible for nanovectors. SEM analysis after NP expansion validated the enlargement, which was consistent with the optical analysis described previously, where the mean diameter recorded was about 400 nm, confirming the fourfold enlargement of the vectors.

We hypothesize that upsizing was achieved by entrapping the NPs in the meshwork of the gel, which is estimated to be 1–2 nm,[25] thus smaller than NPs. This suggests that the gel retains polymeric NPs, re-sizing them while preserving their spatial organization. Transmission electron microscopy is frequently used to observe NPs, but it has some drawbacks, such as the need for expensive equipment and the difficulty of analyzing NPs in the absence of confinement. SEM, on the other hand, is rarely used in NP analysis because its ordinary resolution is higher than 0.1 µm.

This study describes for the first time an easy protocol to analyze the shape and size of NPs by SEM that can be routinely applied as a first step in NP characterization.

The study also demonstrates the feasibility of super-resolved ExM analysis of NPs in biological samples in vitro and in vivo. The super-resolved analysis indicated that the internalized NPs were mostly distributed in the cytosol, with only a few NG in the nuclei of astrocytes and microglia. The super-resolved subcellular analysis provided impressive detail about the interaction of the NPs with different organelles. Conventional fluorescence microscopy cannot resolve Golgi cisternae, which are <100 nm thick with a dense congregation of ribbon-like structures, or accurately distinguish mitochondria (0.5–1 µm), endosomes (up to 0.5–1 µm), lysosomes (0.1–1.2 µm), or ER structures (up to 60 nm). We examined NG internalization at the subcellular level and found colocalization with early endosomes 1 h after NG exposure of astrocytes. 1 day later, NG was mostly clustered in lysosome-like multivesicular bodies of astrocytes, but not microglia, where they remained distributed in the cytosol. Some NG was reported in the Golgi cisternae of glial cells, but only a few murine astrocytes showed altered Golgi structure, suggesting that in a limited number of cells a large number of internalized NG occupied a substantial place in the cytosol, reducing the space available for the ribbon-like structures of the Golgi.

Mitochondrial staining demonstrated more pronounced significant branch lengths of the mitochondrial network for human astrocytes after exposure to NG. We found a significant increase in the expression of the spot size for PERK signal in murine astrocytes after NG internalization. Unfortunately, we were not able to properly quantify mitochondria in microglia or ER organelles in human microglia or astrocytes.

These results demonstrated some significant alterations for mitochondria or ER in astrocytes, but not for other relevant organelles in the cytosol, but cell viability does not seem to be impaired for astrocytes. However, we cannot exclude other potential metabolic stress.

In vivo analysis demonstrated that we could analyze NPs with nanoresolved resolution in ex vivo spinal cord sections. There was an expansion factor of 4.38 ± 0.27 (mean ± SD) and very limited distortion of the NPs in the sample. NG were internalized in several activated microglia/macrophagic cells and astrocytes 3 days after injection, as demonstrated in vitro, while other cells did not seem to be involved in nanoparticle uptake. NG showed a mostly perinuclear distribution in both microglia/macrophages and astrocytes, in line with in vitro findings.

The ability of the NG to deliver molecules was further evaluated in vitro and in vivo, by administering Rolipram, an anti-inflammatory drug. This treatment reduced the production of inflammatory cytokines such as TNFα in murine microglia and LCN2 in murine astrocytes; whereas there was an increase in CCL2 in murine microglia. This suggests that treating microglia in an early stage can reduce the deleterious pro-inflammatory response. Furthermore, some studies have demonstrated a protective role of the chemokine CCL2 during SCI progression,[7,41] suggesting that increased recruitment of phagocytic microglia/macrophages, as found on 7 DPI after early treatment with Rolipram-loaded NG, can improve motor activity.

We were not able to correlate the degree of motor activity improvement with the amount of myelin preserved. This is consistent with recent research suggesting that there is not always a linear correlation between myelin staining and motor activity improvement.[42]

While we do not have direct evidence of a relationship between NG and oligodendrocytes, we cannot exclude this possibility. Further experiments are needed to investigate this aspect.

However, the more organized distribution of microglia/macrophages suggests that they may have been actively working to limit the spread of the lesion. This, together with the anti-inflammatory action of the treatment, may have temporarily relieved the progressive secondary degeneration that was damaging the neuronal network. In contrast, the later treatment, on 14 DPI, impaired motor function. Ex vivo experiments reported that Rolipram reduced the amount of phagocytic and ameboid microglia/macrophages in the rostral and epicenter tracts of the spinal cord, with significant loss of myelin compared to the untreated group. These results suggest that later treatment did not support recovery, quite likely due to the lack of a consistent glial boundary around the epicenter of the lesion, as recently suggested.[3,4,7]

In conclusion, this study demonstrates that NG can selectively deliver effective drugs to microglia and astrocytes. We found no potential adverse effects of NG at the subcellular level, using an original microscopy approach (ExM) in vitro and ex vivo. Responses to the treatment were different when acting on glial cells at the subacute or chronic stage after SCI, suggesting a time-dependence of drug efficacy related to the progressive inflammatory response. This must be taken into account for future optimized treatment of glial cells after SCI. Furthermore, Rolipram treatment was found to have a more pronounced effect on the number and distribution of microglia than astrocytes in vivo. However, an additive or synergistic effect of microglia and astrocytes on the inflammatory state is also possible, as suggested by in vitro experiments. Therefore, acting on both glia populations may be a promising therapeutic strategy for future studies.

4. Experimental Section

NPs Chemistry and Synthesis: NG conjugated to RhB was synthesized according to the experimental procedure previously described.[14,30,39,43] Briefly, PEG hydroxyl groups were modified with imidazole moieties using CDI (PEG-CDI), and PEI chains decorated with propargyl groups were further functionalized through the copper-catalyzed azide-alkyne Huisgen cycloaddition reaction using Rhodamine B (RhB). Two solutions were prepared separately: the first solution involved dissolving PEG-CDI (200 mg, 0.025 mmol) in CH_2Cl_2 (3 mL), and the second BMone dissolving PEI conjugated with RhB (0.017 mmol) in distilled water (5 mL). Under vigorous stirring, the organic solution was added dropwise to the aqueous system, and the final blend was sonicated for 30 min. The polymeric solution was then stirred for 17 h at 25 °C, with the gradual evaporation of CH_2Cl_2. The aqueous system was then purified through dialysis, and lyophilized, resulting in a red solid (NG-RhB).

PEGylated poly-ϵ-caprolactone-based NPs (PCL) were synthesized as previously described.[15,29] Briefly, HEMA-CL_3 macromonomer was synthesized through ring-opening polymerization of caprolactone initiated by 2-hydroxyethyl methacrylate (HEMA) and using $Sn(Oct)_2$ as catalyst, without solvent. Then, using free radical emulsion polymerization, NPs were prepared preformed in a monomer starved semi-batch emulsion polymerization by loading in the reactor potassium persulfate as initiators, Tween 80 as the surfactant, polyethylene glycol methyl ether methacrylate (HEMA-PEG_{19}); HEMA-CL_3 was added in starved condition together

with HEMA-RhB. The 0.1 µm FS are polystyrene particles based on sulfate microsphere grafted to carboxylic acid groups (Invitrogen, F-8803). Their main features are a high charge, hydrophobicity, and a somewhat porous surface layer which can adsorb proteins and other biomolecules. The NP dimension was checked with DLS and transmission electron microscopy.

SEM Analysis: SEM analysis was done in freeze-dried expanded gels analyzed at 10 kV with Evo 50 EP Instrumentation (Zeiss). SmartPI software was used for the statistical calculation of NP mean dimension.

HRMAS Analysis: ^{1}H spectra and diffusion ordered spectroscopy experiments were all done on a Bruker Avance DRX 500 MHz spectrometer equipped with a dual $^{1}H/^{13}C$ High-Resolution Magic Angle Spinning (HRMAS) probe head for semi-solid samples. The polymer-swollen sample was loaded in a 4 mm ZrO_2 rotor (about 12 µL). A spinning rate of 4 KHz was used to eliminate the dipolar contribution. ^{1}H spectra were acquired with water presaturation and 16 scans. The temperature was set and controlled at 305 K.

Murine Primary Cell Cultures: Primary cell cultures of murine astrocytes and microglia were obtained from the spinal cord of 12 days old C57BL/6J mouse embryos by adapting protocols already used in previous work.[14,30] Spinal cords from the embryos were collected in Dulbecco's phosphate buffered saline (DPBS) 1x (Life Technologies It) and treated with DNAse (Sigma Aldrich) and TrypLE Express Enzyme (Thermo Fisher Scientific). After centrifugation at 8000 *g* for 10 min using a cushion of 4% albumin from bovine serum (BSA, Merck Life Science S.r.l.), a mixed population of neurons/glia was obtained and plated at a density of 25 000 cells cm^{-2} in flasks precoated with poly-L-lysine (10 µg mL^{-1}, Sigma Aldrich). Culture media (1% Pen/Strep, 10% fetal bovine serum (FBS) in Dulbecco's modified Eagle medium (DMEM)) were changed three times a week, and cells were grown to confluence. Granulocyte macrophage colony-stimulating factor (Life Technologies It) was added to the culture media and maintained for 2 weeks to induce microglia/macrophage proliferation, when the glial layer was at confluence, flasks were shaken at 275 rpm in incubator o.n. The microglia were detached from the layer and seeded at a density of 25 000 cells cm^{-2}. To obtain astrocyte-enriched cultures, glial cultures were treated with L-leucine methyl ester (60×10^{-3} M, Sigma Aldrich) for 60 min and after at least 4 days astrocytes were collected using Trypsin-ethylenediaminetetraacetic acid (EDTA, GIBCO, 10× diluted in DPBS 1×) and seeded at a density of 40 000 cells cm^{-2} in 24-well plates precoated with poly-L-lysine.

iPSC-Derived Astrocyte Cultures: Episomal human induced-pluripotent stem cells (iPSC) were obtained from Gibco (Life Technologies, CA, US, Lot V2.0), and cultured in feeder-free conditions in a xeno-free culture medium formulation (StemMACS, iPS-Brew XF, Miltenyi Biotec S.r.l.) and expanded by dissociation with Versene 1x (Thermo Fisher Scientific). Neural precursor cells (NPCs) were derived from iPSC as previously described,[44] by blocking TGF-β/BMP-dependent signaling using small molecules in defined commercial medium (STEMdiff SMADi Induction Kit, STEMCELLS Technologies).

DAY 0: confluent iPSC cultures were enzymatically detached with Accutase (Thermo Fisher Scientific) and disaggregated into single cells which were collected and centrifuged at 300 × *g* for 5 min. Cells were then resuspended in an induction medium with Y-27632 added (1×10^{-6} M, Miltenyi Biotec S.r.l.) and plated in Matrigel-coated (Corning) six-well plates. Media was changed daily to the next passage. NPCs were passed for at least four passages to obtain stable neural induction and expanded with Neural Progenitor Medium (NPM, STEMCELLS Technologies). Astrocytes were obtained from NPC from the sixth to the tenth passage. On day 0 of differentiation, NPCs were plated in Matrigel-coated six-well plates at the density of 1.5×10^{4} cells cm^{-2} in NPM with Y-27632 (1×10^{-6} M).

DAY 1: medium was replaced by astrocytes differentiation medium consisting of: AM basal medium (ScienCell) supplemented with 2% FBS, 1% astrocytes growth supplement (AGS, ScienCell), and 1% penicillin/streptomycin. Astrocyte differentiation was obtained by renewing the medium every other day for 4 weeks. At this point, astrocytes were detached and replated in Matrigel-coated 24-well plates with borosilicate glass coverslips at 10^{4} cells cm^{-2} and maintained for 7 days in astrocyte differentiation medium supplemented with CNTF (10 ng mL^{-1}, Peprotech) and BMP4 (10 ng mL^{-1}, Peprotech) for final maturation, as previously reported.[45]

Differentiation of hPSCs into Microglia: The human pluripotent stem cell (hPSC) lines employed for this study were derived from H9 (WA-09, passage 40–60). The PSCs were cultured in Essential 8 medium (E8, Thermo Fisher Scientific) and expanded by dissociation with EDTA (0.5×10^{-3} M, Thermo Fisher Scientific) and plating on Vitronectin coated dishes (Thermo Fisher Scientific). Cells were maintained at 37 °C and 5% CO_2 and they were routinely tested for mycoplasma and periodically assessed for genomic integrity by karyotyping. This study was approved by the regional ethics committee. Human microglia were generated according to the method developed by Guttikonda et al.[46] In brief, on day 0, hPSCs were dissociated as single cells after 10 min incubation with EDTA (0.5×10^{-3} M) at 37 °C and plated as a high-density monolayer 60 000 cells cm^{-2} in either 24-well (0.5 mL per well) or six-well tissue culture plates coated with Matrigel (1:20) in DMEM/F12.

Day 0: E8 medium + Activin A (7.5 ng mL^{-1}) + BMP4 (30 ng mL^{-1}) + ChiR (3×10^{-6} M) + Y-drug (10×10^{-6} M, ROCK inhibitor).
Day 1: E6 medium + Activin A (10 ng mL^{-1}) + BMP4 (40 ng mL^{-1}) + IWP2 (2×10^{-6} M).
Day 2: E6 medium + Activin A (10 ng mL^{-1}) + BMP4 (40 ng mL^{-1}) + IWP2 (2×10^{-6} M) + FGF2 (20 ng mL^{-1}).
Day 3: Accutase cells for 10 min at 37 °C and plate cells at 60 000 cells cm^{-2} in E6 medium + VEGF (15 ng mL^{-1}) + FGF2 (5 ng mL^{-1}) + Y-drug (10×10^{-6} M) on Matrigel-coated plates.
Day 4: E6 medium + VEGF (15 ng mL^{-1}) + FGF2 (5 ng mL^{-1}).
Days 5–6: E6 medium + VEGF (15 ng mL^{-1}) + FGF2 (5 ng mL^{-1}) + SCF (200 ng mL^{-1}) + IL-6 (20 ng mL^{-1}).
Day 7: E6 medium + SCF (100 ng mL^{-1}) + IL-6 (10 ng mL^{-1}) + TPO (30 ng mL^{-1}) IL-3 (30 ng mL^{-1}).
Day 8: do not change medium.
Day 9: E6 medium + SCF (100 ng mL^{-1}) + IL-6 (10 ng mL^{-1}) + TPO (30 ng mL^{-1}) IL-3 (30 ng mL^{-1}).

On day 10, cells in suspension were collected and cultured in Roswell Park Memorial Institute with 10% FBS, L-glutamine, and penicillin–streptomycin with IL-34 (100 ng mL^{-1}) and M-CSF (10 ng mL^{-1}) o.n. a fibronectin-laminin poly-L-ornithin-coated tissue then cultured for 40–60 days.

Microglia were plated 2.5×10^{3} cell per well in poly L-lysine (10 µg mL^{-1}, Sigma Aldrich) pre-coated 24-well plates in RPMI with 10% FBS, L-glutamine, and penicillin–streptomycin with IL-34 (100 ng mL^{-1}) and M-CSF (10 ng mL^{-1}).

Culture Treatments: Mouse and human microglia were activated with lipopolysaccharides (1 µg mL^{-1}, LPS from *Escherichia coli* 0111:B4; Sigma Aldrich) for 18 h; whereas human astrocytes were activated with of LPS (1 mg mL^{-1}) for 18 h, as previously reported.[15] A1 mouse astrocytes were activated by treatment with a mixed solution of complement 1 q (400 ng mL^{-1}, C1q), tumor necrosis factors-alpha (30 ng mL^{-1}, TNF-α), and interleukin-1 (IL-1) α (3 ng mL^{-1}) for 24 h.[13] After cell activation, 2.5% w/v NG was added to the culture media for 60 min or 24 h. At the end of treatment, cell cultures were fixed with 3.7% paraformaldehyde (VWR International S.r.l) for 15 min and stored at 4 °C until use.

Immunocytochemistry and Cell Staining: Fixed astrocytes and microglia were preincubated with 0.2% Triton X-100 (Sigma Aldrich), 1% FBS (Sigma Aldrich), and PBS (0.01 M) for 1 h. Different primary antibodies were used to stain the cellular organelles: anti-alpha tubulin (cytoskeleton staining, 1:1000, Abcam), anti-Lamp1 (lysosome staining, 1:1000, Abcam), anti-EEA1 (early endosome staining, 1:1000, Abcam), anti-GM130 (Golgi staining, 1:1000, Invitrogen), anti-PERK (endoplasmic reticulum staining, 1:100, Cell Signaling Technology), or anti-TOM20 (mitochondria staining, 1:100, Santa Cruz). Then, cells were incubated for 2 h at room temperature (r.t.) with the primary antibody diluted in 0.2% Triton X-100 (Sigma Aldrich), 1% FBS (Sigma Aldrich), and PBS (0.01 M), and with the appropriate fluorescent secondary antibody (CF660R goat anti-mouse or anti-rabbit, Biotium, Alexa 488 goat anti-mouse, Life Technologies Italia

Fil.) diluted in PBS (0.01 M) for 2 h at r.t. Cell nuclei were then incubated 15 min and labeled with Hoechst 33258 (1:1000, Invitrogen).

Expansion Protocol: The protocol below is based on the work of Boyden and his co-workers and all the information about the procedures and methods is already published.[24,25,28,38] Protein anchoring for cell cultures: the fixed and stained cells were treated with 0.25% glutaraldehyde solution (Sigma Aldrich) in PBS (0.01 M) under continuous stirring for 10 min at r.t. Protein anchoring for spinal cord sections: the spinal cord sections were treated with 1% Acryloyl-X SE (AcX, Life Technologies It) diluted in sodium bicarbonate buffer at pH 8.3 o.n under continuous stirring at r.t. After protein anchoring, the cells or tissues were washed twice for 15 min with PBS (0.01 M). Preparation of the gelling solution: a monomer solution of (0.1 M PBS, 2 M NaCl, 8.625% w/w sodium acrylate, 2.5% w/w acrylamide, 0.15% w/w *N,N'*-methylenebisacrylamide), ammonium persulfate (APS, Thermo Scientific), tetramethylethylenediamine (TEMED, Sigma Aldrich), and 4-hydroxy-2,2,6,6- tetramethylpiperidin-1-oxyl (4-hydroxy-TEMPO, Sigma Aldrich) was prepared and cooled on ice to prevent premature gelation. The gelation chambers were constructed as previously described in literature with two spacers each side. Gel polymerization for cell cultures: TEMED (0.2% w/w) and APS (0.2% w/w) initiator were added to the monomer solution in the gelation chamber. Gel polymerization for spinal cord sections: 4-hydroxy-TEMPO (0.01% w/w), TEMED (0.2% w/w), and APS (0.2% w/w) initiator were added to the monomer solution. The tissue slices were incubated with the solution at 4 °C for 5 min (first step) and for 25 min with a fresh solution (second step).

In order to expand only the nanovectors (2% w/v) NG, PCL and FS (Invitrogen, F-8803) were added directly to the monomer solution and the protocol used for gel polymerization of cell cultures was applied. Finally, the formed gel for all the conditions described was transferred to a humidified incubator at 37 °C for 2 h. After the gelation of the cell cultures, the sample was placed in a dish with 2 mL of digestion buffer (50×10^{-3} M Tris life Technologies, 1×10^{-3} M EDTA Millipore, 0.5% Triton X-100 Sigma Aldrich, 0.8 M guanidine HCl Sigma Aldrich) with addition of proteinase K (2 U mL^{-1}, Thermo Fisher Scientific) for 30 min at r.t. under continuous stirring. The homogenization step was optimized for tissue as recommended by Truckenbrodt et al.[47] The improved digestion buffer was consisted of TRIS (50×10^{-3} M), guanidine HCl (800×10^{-3} M), $CaCl_2$ (2×10^{-3} M), and Triton X-100 (0.5% vol/vol) in double distilled water (ddH2O) pH 8.0, with the addition of the proteinase K (2 U mL^{-1}) (final volume of 2 mL) and the gel was digested at 55 °C for 30 min. Concluding, the digestion buffer was removed and the sample was placed in deionized water for 15 min.

Imaging: Pre-ExM imaging was done with an N-SIM microscope (Nikon) equipped with a 100×/1.49 oil objective and an ANDOR camera (iXon3 EMCCD). Post-ExM imaging was acquired using a Cell^R microscope (Olympus) equipped for 60×/1.20 W magnification and with an ORCA camera (Hamamatsu). To quantify the expansion factor, specimens were imaged pre-ExM and post-ExM on an Olympus epifluorescence microscope with a 10×/0.40 air objective. Expanded slices were sandwiched between coverslips of the appropriate size. Post-processing deconvolution (Huygens Professional version 17.10) was used to improve the contrast and sharpness of images captured using the widefield microscope, and cross-talk between channels was removed with a cross-talk corrector (Huygens Professional). The ExM images were shown scaled to the biological size.

Distortion Analysis: To quantify the distortion between pre- and post-ExM images, the protocol proposed by Chozinski et al. was followed.[33] The open-source software Elastix was used for rigid alignment (rotation, translation, and magnification) of the post-expansion image on the pre-ExM image. A second nonrigid alignment deformed the post-ExM image to obtain the best overlap with the original pre-ExM acquisition. RMS of the distortion was evaluated using a custom-written Mathematica routine.

Expansion Analysis and Quantification: The degree of expansion was calculated by selecting two reference points that could be uniquely identified in both pre- and post-ExM images. The distance between these two points was found and the ratio of the pre- and post-ExM measurement was calculated. For the potential deformation, a published protocol was used to calculate the image distortion.[33] Diameters of single NPs pre- and post-ExM were calculated as the distance between two points in the widefield and the SEM images.

Colocalization between NG-RhB (red signal) and early-endosome EEA1 (green signal) was detected with Pearson's coefficient. The diameter of the EEA1 fluorescence signal was calculated as the diameter of the Gaussian beam at FWHM, by Fiji software. Frequency distribution of NG size in lysosomal vesicles stained with LAMP1 was quantified by Imaris bitplane software (spot module). The Golgi apparatus was stained with anti-GM130 antibodies. The supposed reorganization following massive uptake was analyzed in pre-ExM. Using imageJ grid overlay plugin, a lines grid (area per point 1 500 000 μm^2) and randomly selected ten of the resulting squares for subsequent quantifications were superimposed. For each square, a cell count was made using the spot module of Imaris bitplane software and then the cells were identified with an NP signal peak with the thresholding technique of ImageJ.

Only 10.87% of the cells had over-internalization and about 90% of these had undergone a rearrangement of the Golgi apparatus. The rearrangement of the Golgi apparatus in post-ExM was quantitatively examined. 3D quantification of Golgi apparatus volume was done in vitro with Imaris bitplane software (Surface module) once the Z stack image was imported and aligned (Fiji software, Linear Stack Alignment with SIFT plugin). Mitochondrial morphological parameters, in five to nine cells per group, were calculated using freely available plug-in macro Mitochondrial Network Analysis (MiNA).[48] Compartment organization of ER was analyzed in eight to ten cells per group with the spot detection function of Imaris bitplane software (Bitplane, spot module), measuring the spot area.

To obtain a higher quality image and reduce disturbance factors for quantification, a deconvolution algorithm (Huygens professional) was applied before assessment.

Animal Care: All procedures involving care and use of laboratory animals were conducted in conformity with Italian Governing Law (D.lgs 26/2014; Authorization n.19/2008-A issued March 6, 2008 by the Ministry of Health); the NIH Guide for the Care and Use of Laboratory Animals (2011 edition) and EU directives and guidelines (EEC Council Directive 2010/ 63/UE). In addition, the Istituto di Ricerche Farmacologiche Mario Negri IRCCS provided internal authorization for persons conducting animal experiments (Quality Management Certificate—UNI EN ISO 9001:2015—Reg. No. 6121).

Surgery: B6.Cg-Tg(Thy1-YFP)HJrs/J or C57BL/6J – B6.129P-Cx3cr1tm1Litt/J mice (Charles River Laboratories International, Inc.) were used for in vivo and ex vivo studies. Briefly, animals were placed in an anesthesia chamber for 5–10 min until loss of reflexes, and anesthesia was maintained with 2% isoflurane in oxygen throughout the operation. Then, the mice, under isoflurane anesthesia, were placed on a Cunningham Spinal Cord Adaptor (Stoelting, Dublin, Ireland) and mounted on a stereotaxic frame. The spinal cord was exposed and a laminectomy was made at the T12 vertebra. Only to investigate the presence of nanoparticles in the damaged spinal cord, inflammation was induced in the right hemisection of the medulla by three intraparenchymal injections (0.250 µL each) of a mix containing LPS (1 mg mL^{-1}; lipopolysaccharides from *E. coli* O11:B4, Merck Life Science s.r.l.), Hoechst 33258 (10 µg mL^{-1}, Invitrogen), and NG (2.5% w/v) with a glass capillary.

To test the efficacy of an anti-inflammatory drug, Rolipram, loaded into NG, the trauma was induced using a compressive model of SCI. Mice, under isoflurane anesthesia, were placed on a Cunningham Spinal Cord Adaptor (Stoelting, Dublin, Ireland) and mounted on a stereotaxic frame. The spinal cord was exposed and a laminectomy was made at the T12 vertebra. Mechanical trauma of the spinal cord at T12 was induced using an aneurysm clip (2Biological Instruments snc, cat. no. 14120) with a force of 30 g (left in place for 1 min).

After spinal cord compression, dorsal muscles were juxtaposed using absorbable sutures, and the skin sutured. 1 day after the first surgery for subacute treatment, or 14 DPI for subacute treatment, the spinal cord of SCI mice was exposed and NG or NG loaded with Rolipram was injected intraparenchymally. Six 0.250 µL injections were done with a glass capil-

lary (outer diameter 40 ± 2 µm) to cover the injured area. The capillary was positioned ±0.5 mm from the midline, then it was pushed into the parenchyma to 0.6 mm below the pia mater. After each treatment, dorsal muscles were juxtaposed, the skin was sutured and disinfected.

Finally, after the surgery the animals were placed in separate cages for recovery with food and water ad libitum.

Behavioral Assessment: Mice after the treatments were examined by testing hind-limb locomotor performances using the BMS[49] once a week from 7 to 28 DPI (for early subacute treatment) or 35 DPI (for subacute treatment). The BMS is a 10-point scale where 9 means normal locomotion and 0 means complete hind limb paralysis. Behavioral analysis was conducted in an open field arena and was made for video acquisition of the locomotor performances (5 min) with a camera (Denver, ACG-8050 W). Two independent observers, blinded to the treatments, evaluated the videos. Individual hindlimb scores were averaged for each animal group at each time point (every week).

Real-Time Reverse Transcription Polymerase Chain Reaction (RT-PCR): The microglia and astrocytes cultures were activated for about 24 h with LPS (1 µg mL^{-1}) or 3 factors, and then treated with NG or NG-Rolipram. The next day, the cells were collected with QIAzol Lysis Reagent and lysed with a P1000 pipette. Total RNA was extracted using a miRNeasy kit (Qiagen). Briefly, after adding chloroform to the homogenate, the aqueous phase was carefully extracted, loaded onto a column of RNeasy and 450 mL of absolute ethanol was added. Several washes with the buffers according to the manufacturer's directions and then the RNA was eluted in safelock tubes. To eliminate any contaminating genomic DNA, the samples were treated with DNAse (Applied Biosystems) before to the retrotranscription phase with random hexamer primers using Multi-Scribe Reverse Transcriptase (Taq-Man Reverse transcription reagents; Applied Biosystems). RT-PCR was made using 4 ng cDNA, 200 nmol of each primer, and SYBR Green master mix (Applied Biosystems) in a total volume of 22 µL. PCR product levels were measured using green SYBR fluorescence collected during real-time RT-PCR on an applied Biosystems 7300 system. β-Actin was used as reference gene and relative expression levels were recorded according to the manufacturer's ΔΔCT method (Applied Biosystems). Data were expressed as the fold change from noninflamed and nontreated cells (CTR condition).The expression of the following genes was analyzed:

β-Actin: Fw: CGAGCACAGCTTCTTT; Rev: GCAGGTGTCCAT

Tnfa: Fw: TGTGCTCAGAGCTTTCAACAA; Rev: CTTGATGGTGGTGCATGAGA

Lcn2: Fw: TTTGTTCCAAGCTCCAGGGC; Rev: TGGCGAACTGGTTGTAGTCC

CCL2: Fw: GCCTGCTGTTCACAGTTGC; Rev: ATTGGGATCATCTTGCTGGT

Spinal Cord Transcardial Perfusion: To assess the NG internalization, mice were euthanized 3 days after injections. Briefly, under deep anesthesia (IMALGENE, 100 mg kg^{-1} and DOMITOR, 1 mg kg^{-1}) mice were transcardially perfused for 4 min with 40 mL of PBS (0.1 mol L^{-1}) and then 50 mL of paraformaldehyde (4% PAF) solution (VWR International S.r.l) for 5 min. Spinal cords were extracted and post-fixed o.n in PAF (4%) at 4 °C. Tissues were transferred to sucrose (30% Carlo Erba Reagents S.r.l Dasit Group) and stored at 4 °C until use.

Immunohistochemistry: The lesion area was isolated with a blade. The spinal cords were frozen in N-pentane (Carlo Erba Reagents S.r.l Dasit Group) at −45 °C for 3 min, then mounted on a cryostat using optimal cutting temperature compound. For expansion and NG internalization analysis, the frozen tissue was sectioned coronally at 30 µm, starting about 6 mm rostrally to the epicenter. The sections were then directly collected on microscope slides. For neuropathological analysis, the frozen tissue was sectioned sagittally at 30 µm thickness. The sections were collected in a 24-well plate already filled with PBS (0.01 M). Coronal or sagittal sections were preincubated with Triton X-100 (0.1% Sigma Aldrich), NGS (1% Sigma Aldrich), and PBS (0.01 M) for 1 h. Then the sections were incubated overnight at 4 °C with primary antibody directed against astrocytes (Anti-Glial Fibrillary Acidic Protein antibody produced in rabbit (GFAP); 1:500 dilution, Sigma Aldrich) or microglia/macrophages (Rat Anti-mouse CD11b; 1:500 dilution, BIO-RAD) dissolved in PBS (0.01 M), with the addition of normal goat serum (1% Sigma Aldrich) and Triton X-100 (0.1% Sigma Aldrich) . The next day, the fluorescence was detected using a secondary fluorescence antibody (1:250, Alexa 488 goat anti-rabbit, Life Technologies Italia Fil. or CF488A Donkey anti-rat; Biotium) in PBS (0.01 M), incubating the slices for 2 h at r.t. FluoroMyelin Fluorescent Myelin Stains (FM 1:200, Life Technologies Italia Fil.) stain was done on sagittal sections of the spinal cord. The sections were incubated with FM (1:200) in PBS (0.01 M) for 1 h, then washed twice with PBS (0.01 M). Cell nuclei were labeled with Hoechst 33258 (1:1000, Invitrogen) by 15 min incubation.

Neuropathological Analysis: For neuropathological analysis, microglia/macrophages (stained with CD11b antibody) or astrocyte activation (stained with GFAP antibody) were analyzed in sagittal sections of spinal cords. Two different time points were used for each treatment: 7 DPI for the early subacute phase and 35 DPI for the subacute phase. Sections were acquired using a Cell^R microscope and a 20 magnification. The area acquired covered the whole lesion area (using the same number of frames in the *y*-direction) and added four *z*-stacks, each 1 µm apart.

AI Pipeline: The pipeline used a U-Net[50] deep neural network, which was a state-of-the-art architecture specifically designed for biomedical image segmentation. It employed a sequence of downsampling layers followed by a sequence of upsampling layers that increased the shape to the original one, and a set of skip connections that fed the deep layers with contextual information from the shallow layers. First, the network was trained on a subset of manually curated cell regions-of-interest in order to recognize the shape of microglia and astrocyte cells. Then trained models were used to segment cell images in the whole dataset. To separate cells that appeared stuck together in high-intensity regions, a custom cell separation algorithm was implemented. First, "true" nuclei cells were recognized with cluster analysis. Then nuclei cells were overlapped with the other cell channel to identify true regions of microglia/astrocyte cells. Finally, the corresponding nuclei cells were expanded with a multistep, and multilabel dilation algorithm that starts expanding nuclei boundaries and stops when the borders encounter other growing cells or the background. The final result was an image of nonoverlapping labeled cells. All AI-generated data were analyzed and quantified with Tableau Software.

Statistical Analysis: Data analysis was done with Prism software (Graphpad). All data were preprocessed by eliminating outliers, calculated using Graphpad Outlier calculator (alpha = 0.05). To test the differences, analysis of variance and a nonparametric *t*-test were used. Post hoc tests were used to identify specific group differences. *p*-Value <0.05 was considered significant for all analyses. Colocalization was measured with Pearson's coefficient and evaluated using Imaris Software (Bitplane). Data were presented as mean ± SD or SEM.

Supporting Information

Supporting Information is available from the Wiley Online Library or from the author.

Acknowledgements

V.V. and E.P. contributed equally to this work. Authors' research was supported by Amici del Mario Negri charity, Politecnico di Milano grants and in part by the italian project CNRBIOMICS PON R&I PIR01_00017.

Open access funding provided by BIBLIOSAN.

Conflict of Interest

The authors declare no conflict of interest.

Data Availability Statement

The data that support the findings of this study are available from the corresponding author upon reasonable request.

Keywords

glial cells, nanoparticles, spinal cord injury, super-resolution microscopy

Received: August 2, 2023
Revised: November 10, 2023
Published online: December 2, 2023

[1] C. S. Ahuja, J. R. Wilson, S. Nori, M. R. N. Kotter, C. Druschel, A. Curt, M. G. Fehlings, *Nat. Rev. Dis. Primers* **2017**, *3*, 17018.
[2] J. H. Badhiwala, C. S. Ahuja, M. G. Fehlings, *J. Neurosurg.* **2019**, *30*, 1.
[3] X. Zhou, S. Wahane, M.-S. Friedl, M. Kluge, C. C. Friedel, K. Avrampou, V. Zachariou, L. Guo, B. Zhang, X. He, R. H. Friedel, H. Zou, *Nat. Neurosci.* **2020**, *23*, 337.
[4] V. Bellver-Landete, F. Bretheau, B. Mailhot, N. Vallières, M. Lessard, M.-E. Janelle, N. Vernoux, M.-È. Tremblay, T. Fuehrmann, M. S. Shoichet, S. Lacroix, *Nat. Commun.* **2019**, *10*, 518.
[5] I. B. Wanner, M. A. Anderson, B. Song, J. Levine, A. Fernandez, Z. Gray-Thompson, Y. Ao, M. V. Sofroniew, *J. Neurosci.* **2013**, *33*, 12870.
[6] F. H. Brennan, J. C. E. Hall, Z. Guan, P. G. Popovich, *Neurosci.* **2018**, https://doi.org/10.1101/410258.
[7] F. H. Brennan, Y. Li, C. Wang, A. Ma, Q. Guo, Y. Li, N. Pukos, W. A. Campbell, K. G. Witcher, Z. Guan, K. A. Kigerl, J. C. E. Hall, J. P. Godbout, A. J. Fischer, D. M. Mctigue, Z. He, Q. Ma, P. G. Popovich, *Nat. Commun.* **2022**, *13*, 4096.
[8] L. M. Milich, J. S. Choi, C. Ryan, S. R. Cerqueira, S. Benavides, S. L. Yahn, P. Tsoulfas, J. K. Lee, *J. Exp. Med.* **2021**, *218*, e20210040.
[9] S. A. Liddelow, B. A. Barres, *Immunity* **2017**, *46*, 957.
[10] C. Escartin, E. Galea, A. Lakatos, J. P. O'callaghan, G. C. Petzold, A. Serrano-Pozo, C. Steinhäuser, A. Volterra, G. Carmignoto, A. Agarwal, N. J. Allen, A. Araque, L. Barbeito, A. Barzilai, D. E. Bergles, G. Bonvento, A. M. Butt, W.-T. Chen, M. Cohen-Salmon, C. Cunningham, B. Deneen, B. De Strooper, B. Díaz-Castro, C. Farina, M. Freeman, V. Gallo, J. E. Goldman, S. A. Goldman, M. Götz, A. Gutiérrez, et al., *Nat. Neurosci.* **2021**, *24*, 312.
[11] M. Hara, K. Kobayakawa, Y. Ohkawa, H. Kumamaru, K. Yokota, T. Saito, K. Kijima, S. Yoshizaki, K. Harimaya, Y. Nakashima, S. Okada, *Nat. Med.* **2017**, *23*, 818.
[12] Q.-M. Pang, S.-Y. Chen, Q.-J. Xu, M. Zhang, D.-F. Liang, S.-P. Fu, J. Yu, Z.-L. Liu, Q. Zhang, T. Zhang, *Int. Immunopharmacol.* **2022**, *108*, 108754.
[13] S. A. Liddelow, K. A. Guttenplan, L. E. Clarke, F. C. Bennett, C. J. Bohlen, L. Schirmer, M. L. Bennett, A. E. Münch, W.-S. Chung, T. C. Peterson, D. K. Wilton, A. Frouin, B. A. Napier, N. Panicker, M. Kumar, M. S. Buckwalter, D. H. Rowitch, V. L. Dawson, T. M. Dawson, B. Stevens, B. A. Barres, *Nature* **2017**, *541*, 481.
[14] I. Vismara, S. Papa, V. Veneruso, E. Mauri, A. Mariani, M. De Paola, R. Affatato, A. Rossetti, M. Sponchioni, D. Moscatelli, A. Sacchetti, F. Rossi, G. Forloni, P. Veglianese, *ACS Nano* **2020**, *14*, 360.
[15] S. Papa, I. Caron, E. Erba, N. Panini, M. De Paola, A. Mariani, C. Colombo, R. Ferrari, D. Pozzer, E. R. Zanier, F. Pischiutta, J. Lucchetti, A. Bassi, G. Valentini, G. Simonutti, F. Rossi, D. Moscatelli, G. Forloni, P. Veglianese, *Biomaterials* **2016**, *75*, 13.
[16] M. A. Anderson, J. E. Burda, Y. Ren, Y. Ao, T. M. O'shea, R. Kawaguchi, G. Coppola, B. S. Khakh, T. J. Deming, M. V. Sofroniew, *Nature* **2016**, *532*, 195.
[17] M. V. Sofroniew, *Nat. Rev. Neurosci.* **2015**, *16*, 249.
[18] S. Okada, M. Hara, K. Kobayakawa, Y. Matsumoto, Y. Nakashima, *Neurosci. Res.* **2018**, *126*, 39.
[19] X. Freyermuth-Trujillo, J. J. Segura-Uribe, H. Salgado-Ceballos, C. E. Orozco-Barrios, A. Coyoy-Salgado, *Cells* **2022**, *11*, 2692.
[20] S. Papa, F. Rossi, I. Vismara, G. Forloni, P. Veglianese, *ACS Chem. Neurosci.* **2019**, *10*, 1173.
[21] B. D. Kevadiya, B. M. Ottemann, M. B. Thomas, I. Mukadam, S. Nigam, J. Mcmillan, S. Gorantla, T. K. Bronich, B. Edagwa, H. E. Gendelman, *Adv. Drug Delivery Rev.* **2019**, *148*, 252.
[22] D. Vanhecke, L. Rodriguez-Lorenzo, M. J. Clift, F. Blank, A. Petri-Fink, B. Rothen-Rutishauser, *Nanomedicine* **2014**, *9*, 1885.
[23] L. Schermelleh, A. Ferrand, T. Huser, C. Eggeling, M. Sauer, O. Biehlmaier, G. P. C. Drummen, *Nat. Cell Biol.* **2019**, *21*, 72.
[24] S. Alon, G. H. Huynh, E. S. Boyden, *FEBS J.* **2019**, *286*, 1482.
[25] F. Chen, P. W. Tillberg, E. S. Boyden, *Science* **2015**, *347*, 543.
[26] M. Igarashi, M. Nozumi, L.-G. Wu, F. Cella Zanacchi, I. Katona, L. Barna, P. Xu, M. Zhang, F. Xue, E. Boyden, *J. Neurosci.* **2018**, *38*, 9459.
[27] B. R. Gallagher, Y. Zhao, *Neurobiol. Dis.* **2021**, *154*, 105362.
[28] P. W. Tillberg, F. Chen, K. D. Piatkevich, Y. Zhao, C.-C. Yu, B. P. English, L. Gao, A. Martorell, H.-J. Suk, F. Yoshida, E. M. Degennaro, D. H. Roossien, G. Gong, U. Seneviratne, S. R. Tannenbaum, R. Desimone, D. Cai, E. S. Boyden, *Nat. Biotechnol.* **2016**, *34*, 987.
[29] S. Papa, F. Rossi, R. Ferrari, A. Mariani, M. De Paola, I. Caron, F. Fiordaliso, C. Bisighini, E. Sammali, C. Colombo, M. Gobbi, M. Canovi, J. Lucchetti, M. Peviani, M. Morbidelli, G. Forloni, G. Perale, D. Moscatelli, P. Veglianese, *ACS Nano* **2013**, *7*, 9881.
[30] S. Papa, V. Veneruso, E. Mauri, G. Cremonesi, X. Mingaj, A. Mariani, M. De Paola, A. Rossetti, A. Sacchetti, F. Rossi, G. Forloni, P. Veglianese, *J. Controlled Release* **2021**, *330*, 218.
[31] S. Papa, R. Ferrari, M. De Paola, F. Rossi, A. Mariani, I. Caron, E. Sammali, M. Peviani, V. Dell'oro, C. Colombo, M. Morbidelli, G. Forloni, G. Perale, D. Moscatelli, P. Veglianese, *J. Controlled Release* **2014**, *174*, 15.
[32] P. W. Tillberg, F. Chen, *Annu. Rev. Cell Dev. Biol.* **2019**, *35*, 683.
[33] T. J. Chozinski, A. R. Halpern, H. Okawa, H.-J. Kim, G. J. Tremel, R. O. L. Wong, J. C. Vaughan, *Nat. Methods* **2016**, *13*, 485.
[34] M.-E. Tremblay, I. Zhang, K. Bisht, J. C. Savage, C. Lecours, M. Parent, V. Titorenko, D. Maysinger, *J. Neuroinflammation* **2016**, *13*, 116.
[35] G. Feng, R. H. Mellor, M. Bernstein, C. Keller-Peck, Q. T. Nguyen, M. Wallace, J. M. Nerbonne, J. W. Lichtman, J. R. Sanes, *Neuron* **2000**, *28*, 41.
[36] A. T. Wassie, Y. Zhao, E. S. Boyden, *Nat. Methods* **2019**, *16*, 33.
[37] A. Klimas, Y. Zhao, *ACS Nano* **2020**, *14*, 7689.
[38] S. M. Asano, R. Gao, A. T. Wassie, P. W. Tillberg, F. Chen, E. S. Boyden, *Curr. Protoc. Cell Biol.* **2018**, *80*, e56.
[39] E. Mauri, I. Moroni, L. Magagnin, M. Masi, A. Sacchetti, F. Rossi, *React. Funct. Polym.* **2016**, *105*, 35.
[40] E. D. Karagiannis, J. S. Kang, T. W. Shin, A. Emenari, S. Asano, L. Lin, E. K. Costa, I. M. A. X. T. Grand Challenge Consortium, A. H. Marblestone, N. Kasthuri, E. S. Boyden, *bioRxiv* **2019**, https://doi.org/10.1101/829903.
[41] S. Papa, I. Vismara, A. Mariani, M. Barilani, S. Rimondo, M. De Paola, N. Panini, E. Erba, E. Mauri, F. Rossi, G. Forloni, L. Lazzari, P. Veglianese, *J. Controlled Release* **2018**, *278*, 49.
[42] K. Fouad, P. G. Popovich, M. A. Kopp, J. M. Schwab, *Nat. Rev. Neurol.* **2021**, *17*, 53.
[43] E. Mauri, P. Veglianese, S. Papa, A. Rossetti, M. De Paola, A. Mariani, Z. Posel, P. Posocco, A. Sacchetti, F. Rossi, *Colloids Surf., B* **2020**, *185*, 110574.
[44] M. De Paola, F. Pischiutta, D. Comolli, A. Mariani, J. Kelk, I. Lisi, M. Cerovic, S. Fumagalli, G. Forloni, E. R. Zanier, *J. Cereb. Blood Flow Metab.* **2023**, *43*, 680.
[45] V. C. Jones, R. Atkinson-Dell, A. Verkhratsky, L. Mohamet, *Cell Death Dis.* **2017**, *8*, e2696.
[46] S. R. Guttikonda, L. Sikkema, J. Tchieu, N. Saurat, R. M. Walsh, O. Harschnitz, G. Ciceri, M. Sneeboer, L. Mazutis, M. Setty, P. Zumbo, D. Betel, L. D. De Witte, D. Pe'er, L. Studer, *Nat. Neurosci.* **2021**, *24*, 343.

[47] S. Truckenbrodt, C. Sommer, S. O. Rizzoli, J. G. Danzl, *Nat. Protoc.* **2019**, *14*, 832.
[48] A. J. Valente, L. A. Maddalena, E. L. Robb, F. Moradi, J. A. Stuart, *Acta Histochem.* **2017**, *119*, 315.
[49] D. M. Basso, L. C. Fisher, A. J. Anderson, L. B. Jakeman, D. M. Mctigue, P. G. Popovich, *J. Neurotrauma* **2006**, *23*, 635.
[50] O. Ronneberger, P. Fischer, T. Brox, in *Medical Image Computing and Computer-Assisted Intervention – MICCAI 2015* (Eds: N. Navab, J. Hornegger, W. M. Wells, A. F. Frangi), Springer International Publishing, Cham **2015**, pp. 234–241.